ENGINEERING

In situ diagnosis and simultaneous treatment of cardiac diseases using a single-device platform

Jae Chul Hwang[1,2]†, Moohyun Kim[1,2]†, Sumin Kim[1,2], Hunkyu Seo[1,2], Soohwan An[2,3], Eui Hwa Jang[4], Seung Yeop Han[2,3], Mi Jung Kim[1,5], Nam Kyun Kim[4], Seung-Woo Cho[2,3]*, Sak Lee[4]*, Jang-Ung Park[1,2,5]*

The in situ diagnosis of cardiac activities with simultaneous therapeutic electrical stimulation of the heart is key to preventing cardiac arrhythmia. Here, we present an unconventional single-device platform that enables in situ monitoring even in a wet condition and control of beating heart motions without interferences to the recording signal. This platform consists of the active-matrix array of pressure-sensitive transistors for detecting cardiac beatings, biocompatible, low-impedance electrodes for cardiac stimulations, and an alginate-based hydrogel adhesive for attaching this platform conformally to the epicardium. In contrast to conventional electrophysiological sensing using electrodes, the pressure-sensitive transistors measured mechanophysiological characteristics by monitoring the spatiotemporal distributions of cardiac pressures during heart beating motions. In vivo tests show mechanophysiological readings having good correlation with electrocardiography and negligible interference with the electrical artifacts caused during cardiac stimulations. This platform can therapeutically synchronize the rhythm of abnormal heartbeats through efficient pacing of cardiac arrhythmia.

INTRODUCTION

Sudden cardiac death (SCD), a symptomless, fast-acting failure of the heart (within 1 hour) due to a cardiac abnormality, is a common and fatal occurrence that accounts for more than 60% of the deaths associated with cardiovascular disease (1–3). The main cause of SCD is cardiac arrhythmia, which accounts for about 80% of the SCDs (4). During the arrhythmia, the heart can beat too fast (tachycardia), too slowly (bradycardia), or with an irregular rhythm (fibrillation). Continuous monitoring of cardiac activity and its immediate treatment are the key to preventing arrhythmia-related sudden death when an arrhythmia occurs (5, 6). Therefore, various efforts have led to the development of cardiac implantable electronic devices (CIEDs) that are capable of diagnosing and treating arrhythmia. For example, permanent pacemakers and implantable cardioverter-defibrillators, which are representative commercial CIEDs, can be inserted into the human body for a longer duration to monitor cardiac activity (7). If a cardiac abnormality occurs, these CIEDs provide immediate electrical impulses that can pace the rhythm of the heart to its original value. However, implanting these bulky, rigid devices requires the insertion of their pulse generator into the body and lead electrodes into the cardiac chambers through the delicate subclavian vein. This involves complicated surgical procedures that can cause multiple postoperative complications, such as the regurgitation of the tricuspid valve, the perforation of veins, and ischemic inflammation (8–10). Recently, functional cardiac patches are emerging as a promising research field as they not only investigate cardiac

activity such as electrocardiography but also have the potential to restore cardiac functions through clinical therapeutic methods such as myocardium regeneration (11). In particular, cardiac patch devices, which are attached directly to the curvilinear epicardial surface, also have been demonstrated for diagnosing electrophysiological abnormalities in the heart through real-time spatiotemporal mapping of the conduction of heart chambers or treating heart abnormality by electrical stimulation. These devices present a promising strategy to diagnose the electrophysiological abnormalities in the heart through spatiotemporal mapping of the conduction of heart chambers or treat abnormality by electrical stimulation (12–20).

Cardiac electrophysiology is a branch of physiology that pertains to the electrical activity of cardiomyocytes, and it has been used extensively as the standard recording method to analyze the contraction and relaxation of the cardiac muscles. Briefly, waves of electrical pulses that are initiated at the sinoatrial (SA) node induce a series of physical contractions and relaxations in the myocardium. This process allows blood to be circulated throughout the body, and various cardiac diseases can result from the dynamic irregularities within the heart and blood vessels. Although both implantable CIEDs and attachable patch-type devices mainly detect the heart's electrical conduction system in the form of an electrocardiogram (ECG), the ECG signals are affected directly by electromagnetic interferences and other stimulators. These ECG artifacts can lead to the misinterpretation of cardiac activity and result in unnecessary medical treatment with potentially fatal outcomes (21). To address this limitation, these devices are configured to have separate monitoring and stimulation components, which make them bulky and complicated, or they have to operate the monitoring and stimulation sequentially because of their difficulties in monitoring the simultaneous function of both the ECG and electrical stimulation for the immediate treatment of cardiac abnormalities (22–25). In addition to the interpretation of the heart's electrical activity using ECG analysis, the direct measurement of cardiac mechanical movements during the contraction and relaxation cycles can also provide vital information that can be used to understand SCDs. For example, the direct contact of

[1]Department of Materials Science and Engineering, Yonsei University, Seoul 03722, Republic of Korea. [2]Center for Nanomedicine, Institute for Basic Science (IBS), Yonsei University, Seoul 03722, Republic of Korea. [3]Department of Biotechnology, Yonsei University, Seoul 03722, Republic of Korea. [4]Division of Cardiovascular Surgery, Severance Cardiovascular Hospital, Yonsei University College of Medicine, Yonsei University Health System, Seoul 03722, Republic of Korea. [5]KIURI Institute, Yonsei University, Seoul 03722, Republic of Korea.
*Corresponding author. Email: jang-ung@yonsei.ac.kr (J.-U.P.); sak911@yuhs.ac.kr (S.L.); seungwoocho@yonsei.ac.kr (S.-W.C.)
†These authors contributed equally to this work.

a bulky singlet vibrator to the surface of a heart to measure its myocardial elastance as well as a catheter or a cardiac sleeve for indicating the conformal contact between these instruments and cardiac tissues have been demonstrated previously (26–29). Although these mechanical sensors were useful for assisting surgical instruments, they could not diagnose physiological abnormalities in a heart for the direct treatment of arrhythmia.

To overcome these limitations, we present an unconventional approach for the fabrication of a single-device platform that is conformably attachable to the wet surface of a heart for use in the in situ monitoring and control of cardiac beating motions. In contrast to electrophysiological recording, this device platform can present mechanophysiological analysis by using pressure sensors to directly monitor relative changes in cardiac pressures. This platform is composed of three components: (i) an active-matrix array of pressure-sensitive air-dielectric transistors (as pressure sensors) for detecting cardiac physical activities, (ii) pacing electrodes for therapeutic electrical stimulation, and (iii) an alginate-based hydrogel adhesive patch for conformal attachment of this device platform to the cardiac epicardium. The key advantages of this platform are as follows: (i) the use of an active-matrix pressure sensor array (100 sensing nodes) to analyze the mechanical movement during the cyclic cardiac beating, such as its contraction and relaxation in the form of a real-time, spatiotemporal, two-dimensional (2D) map. The 10×10 sensing nodes were designed to have a pixel resolution of 1 mm, capturing the branch of arterial blood vessels (such as left coronary arteries, which are about 1 mm in rabbits) as well as the overall pressure distribution on the cardiac surface at a given spatial resolution. The variation of the pressure of the cardiac physical motions that are recorded using this platform can correspond to ECG traces and can generate negligible artifacts in the sensing signal even when an electrical impulse is delivered for pacing the heart. (ii) Its modulation of cardiac beating: This pressure sensor array is also integrated with biocompatible pacing electrodes on which platinum (Pt) black nanoparticles are coated uniformly for low impedance and high charge storage capacitance (CSC) characteristics to enable cardiac actuation at low pacing thresholds (0.6 V/mm). These pacing electrodes can synchronize the beating of the heart at a threshold amplitude that is only one-third the amplitudes of conventional pacing electrodes. In addition, (iii) a catechol-functionalized alginate hydrogel is synthesized and lyophilized as a dried biocompatible adhesive patch using a dual-crosslinking mechanism to attach this device platform very quickly (within ~30 s) to the wet and curvilinear surface of an epicardium. This heart-attachable device platform enables its safe and stable operation on the epicardium without notable tissue inflammations. Furthermore, in vivo clinical trials have been conducted on the left ventricular (LV) epicardium of a live rabbit to record cardiac motions continuously in real time. To test the therapeutic application of this platform in disease modeling, expressions of arrhythmias, such as bradycardia and ventricular fibrillations, were developed in the rabbit through the injection of drugs and electrical shocks. As the form of a single-device system, this heart-attachable platform enables simultaneous, corrective treatment through immediate electrical impulses while using its continuous mechanophysiological recording capability to monitor the abnormal cardiac beating motions of arrhythmias. In addition, we also investigated the correlation between cardiovascular hemodynamics and the distribution of the epicardial pressure. The change in blood pressure (BP) and flow in a cardiovascular system, which is a crucial factor of

hemodynamics, further elucidated the complex cardiac dynamics during electrical pacing. On the basis of our in vivo result, this patch device presents a promising strategy to diagnose the abnormalities in the heart through mechanophysiological spatiotemporal mapping of the heart chambers and treat heart abnormality, such as arrhythmias, by electrical stimulation. The potential for using this device platform for in situ mechanophysiological analysis of heart activities and simultaneous electric therapeutics indicates its substantial promise for use beyond the limit of conventional electrophysiological methods. A table that compares and differentiates our device with previous works of cardiac devices is presented in table S1.

RESULTS

Mechanophysiological monitoring using an active-matrix pressure sensor array

Figure 1A illustrates the schematic layout of this heart-attachable, patch-type device platform where an active-matrix array of pressure-sensitive, air-dielectric transistors are integrated with biocompatible pacing electrodes. This patch-type platform is formed by assembling two flexible plastic panels (bottom and top panels) to fabricate the transistor array and pacing electrodes, with encapsulation layers covering the entire outer surface of this flexible patch. The bottom panel consists of the semiconductor channels, source/drain electrodes, and a passivation layer. Separately, the top panel of this device platform consists of top-gate electrodes and a pressure-sensitive elastomeric layer. In the structure of this device platform (total thickness, 38 μm), all of the outer surfaces of this epicardial patch are encapsulated by biocompatible materials such as medical-grade silicone, parylene, and Pt black before its direct attachment to a heart. The detailed fabrication processes related to this device patch are described in the Supplementary Materials and in Materials and Methods.

In a human adult, the heart repeats its cycle of contraction and relaxation 60 to 80 times per minute under normal conditions to pump blood throughout the body. The LV provides systemic circulation, i.e., it relaxes after receiving blood from the left atrium and then contracts to pump blood out of the ventricle. Our patch-like platform can be laminated conformally onto the surface of the LV with its 500-nm-thick parylene encapsulation layer facing the epicardium. Here, the pacing electrodes (Pt black) are contacted directly on the epicardial surface through holes of the parylene layer. As illustrated in Fig. 1A, another patch of the soft alginate hydrogel adhesive covers the entire top outer surface of our device platform as well as the surrounding epicardium area to strengthen its adhesion to the epicardium during cardiac motions. This adhesive layer is not pasted to the interface between the device platform and the epicardium. The active-matrix array of pressure-sensitive air-dielectric transistors (pixel resolution, 1 mm as the distance between adjacent transistors) of this patch-like platform can monitor the relative pressure distributions that are caused by the changes in the volume of the LV during the cardiac cycle in the form of a real-time, spatiotemporal, 2D map. During the process of ventricular relaxation, for example, the blood that is supplied from the left atrium fills the chamber through the mitral valve, and the epicardium of the LV exerts compressive pressure on this device platform as the chamber expands (Fig. 1B). As the corresponding pressure compresses this platform, the air-dielectric layer of the top-gate transistor becomes thinner, and this results in a higher drain current (I_D)
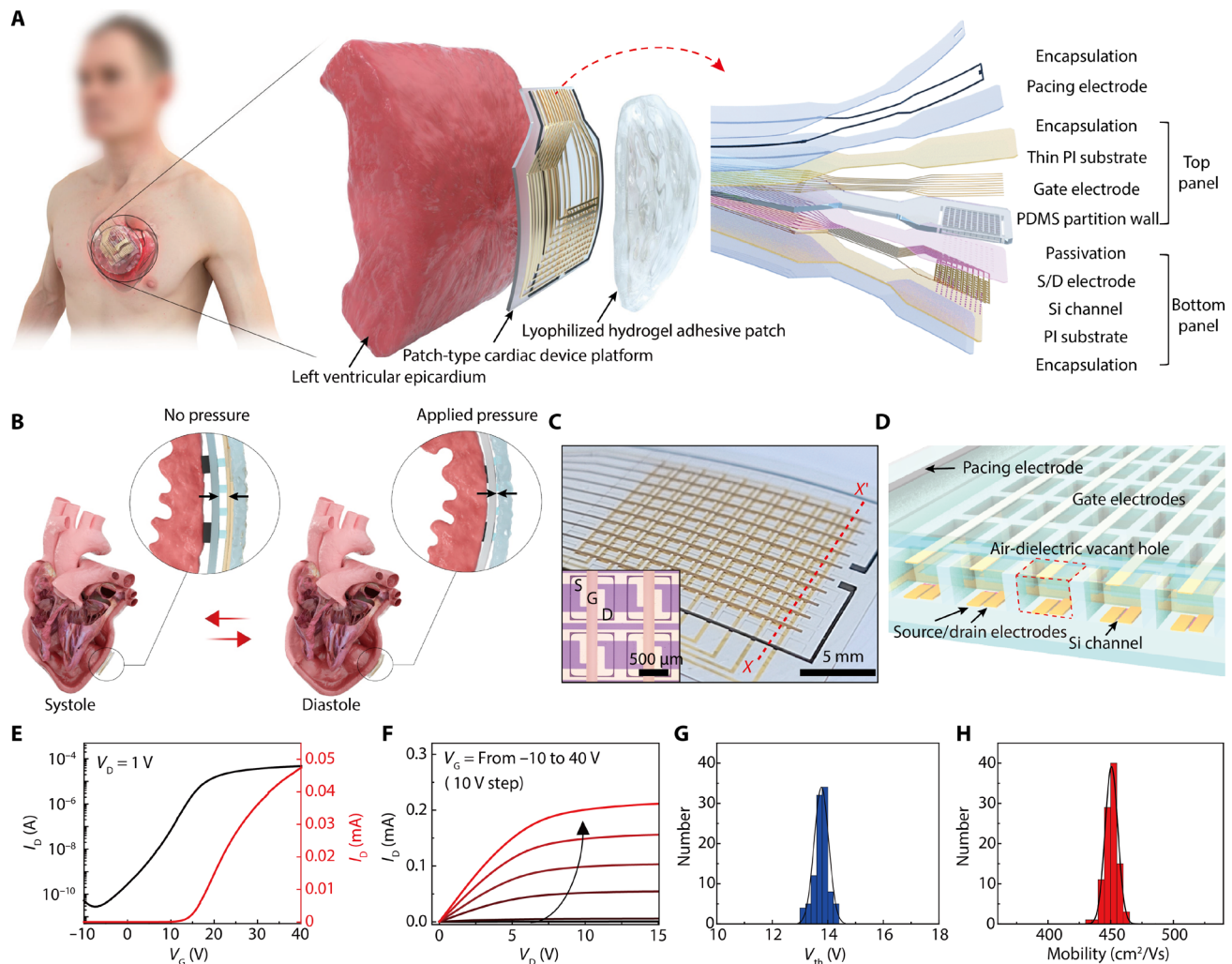
Fig. 1. Heart-attachable patch-type device platform. (**A**) Schematic layouts of the device platform composed of an active-matrix pressure-sensitive transistor array and biocompatible pacing electrodes with encapsulation layers (right inset). This device platform was attached to the epicardium by covering a hydrogel adhesive patch for monitoring cardiac pressure and electrical treatment (left). (**B**) Schematic illustrations on the pressure sensing mechanism using this device platform during cardiac contraction (systole) and relaxation (diastole). (**C**) Photograph of the active-matrix pressure-sensitive transistor array and Pt black pacing electrodes (outer black lines) in the patch device platform. The 10×10 sensing nodes defined by elastomeric partitions are shown in the photograph. The inset shows an optical micrograph of four adjacent transistors that are isolated with elastomeric partitions. S, D, and G denote the source, drain, and gate electrodes, respectively. (**D**) Cross-sectional schematic illustration of the active-matrix air-dielectric transistor array [designated as X-X' in (C)]. A red dashed box indicates the air-dielectric vacant hole that can be compressed when pressure is applied. (**E** and **F**) Representative transfer ($V_D = 1$ V) and output ($V_G = -10$ to 40 V) characteristics of the air-dielectric transistor in this epicardial device patch at ambient conditions. (**G** and **H**) Statistical distributions of the threshold voltage (V_{th}) and the field-effect n-channel mobility of 100 transistors in total, respectively.

due to the increase in capacitance of the gate-air-channel structure. Then, the pressure applied on this device by the epicardium is reduced again during the contraction of the LV, leading to a rapid decrease in the corresponding I_D as a signal of a pressure sensor. Through this underlying mechanophysiological mechanism of the heart, this patch-type platform can detect the cardiac beating cycles and provide the related physical parameters.

Furthermore, the pacing electrodes (Pt black) in this platform come in direct contact with the epicardium. The premeditated electrical pulses, meant to correct the abnormal cardiac conditions, can be transmitted to the heart through the pacing electrodes, which are connected by custom-made flexible flat cables to an external power source. These electrical pulses can trigger systematic muscular contraction by inducing depolarization of cardiac muscle cells with

negligible interference to the pressure signals. In contrast to the conventional systems that must have separate components for monitoring and stimulation due to the interference between the ECG signals and the electrical impulses, both monitoring and stimulation components can be integrated in our epicardial patch as a single-device platform. Therefore, this single platform enables the mechanophysiological monitoring of cardiac beating motions using pressure sensors as well as monitoring synchronized electrical pacing using Pt black electrodes, which can be efficient for in situ cardiac arrhythmia diagnosis and simultaneous treatment.

Figure 1C is a photograph of the pressure-sensitive air-dielectric transistor array (100 sensing nodes) and the pacing electrodes (black-colored lines). The inset optical micrograph shows the source, drain, and gate electrodes of four adjacent transistors, and local air holes

are positioned underneath the gate electrodes. Figure 1D also illustrates a cross-sectional schematic layout of this transistor array, which is indicated as the red dashed line (X-X′) in Fig. 1C. Figure 1 (E and F) shows the representative transfer and output characteristics of the air-dielectric Si transistor at ambient conditions, respectively. The n-channel mobility (μ) was calculated as ~450 cm^2 V^{-1} s^{-1}. The on/off ratio ($I_{on/off}$) of I_D and the threshold voltage (V_{th}) of this transistor were 2×10^6 and 13.8 V, respectively. Through statistical distribution analysis of 100 air-dielectric transistors with their active-matrix integration form, both the threshold voltage and mobility had Gaussian distribution profiles (Fig. 1, G and H). Specifically, low hysteresis is a key feature of this air-dielectric transistor for its operation as a pressure sensor. As shown in fig. S1, this transistor exhibited negligible hysteresis because of the clean interface between the channel and the air gap, which negated charge trapping and chemical interactions (30–34). These characteristics, such as good uniformity and negligible hysteresis, are advantageous to enable reliable

and fast-response capabilities for pressure sensing to detect dynamic and continuous cardiac motions, such as a heartbeat.

Performances of the pressure sensing and pacing components

Figure 2A illustrates the pressure sensing mechanism by the heartbeat using an air-dielectric transistor in the patch-type platform. The application of normal mechanical force on the transistor reduces the thickness of its air-dielectric layer because of the good elasticity of polydimethylsiloxane (PDMS). Therefore, the compressive force by the heartbeat increases the I_D of this transistor due to the increase in the capacitance of the gate-air-channel structure. This pressure-sensitive modulation in I_D enables the individual air-dielectric transistor to act as a pressure sensor. To evaluate the pressure-sensing characteristics, a well-defined load was applied in the pressure range from 1 to 200 kPa using an experimental setup that consisted of a motorized z-axis stage (Mark-10 ESM 303) and a
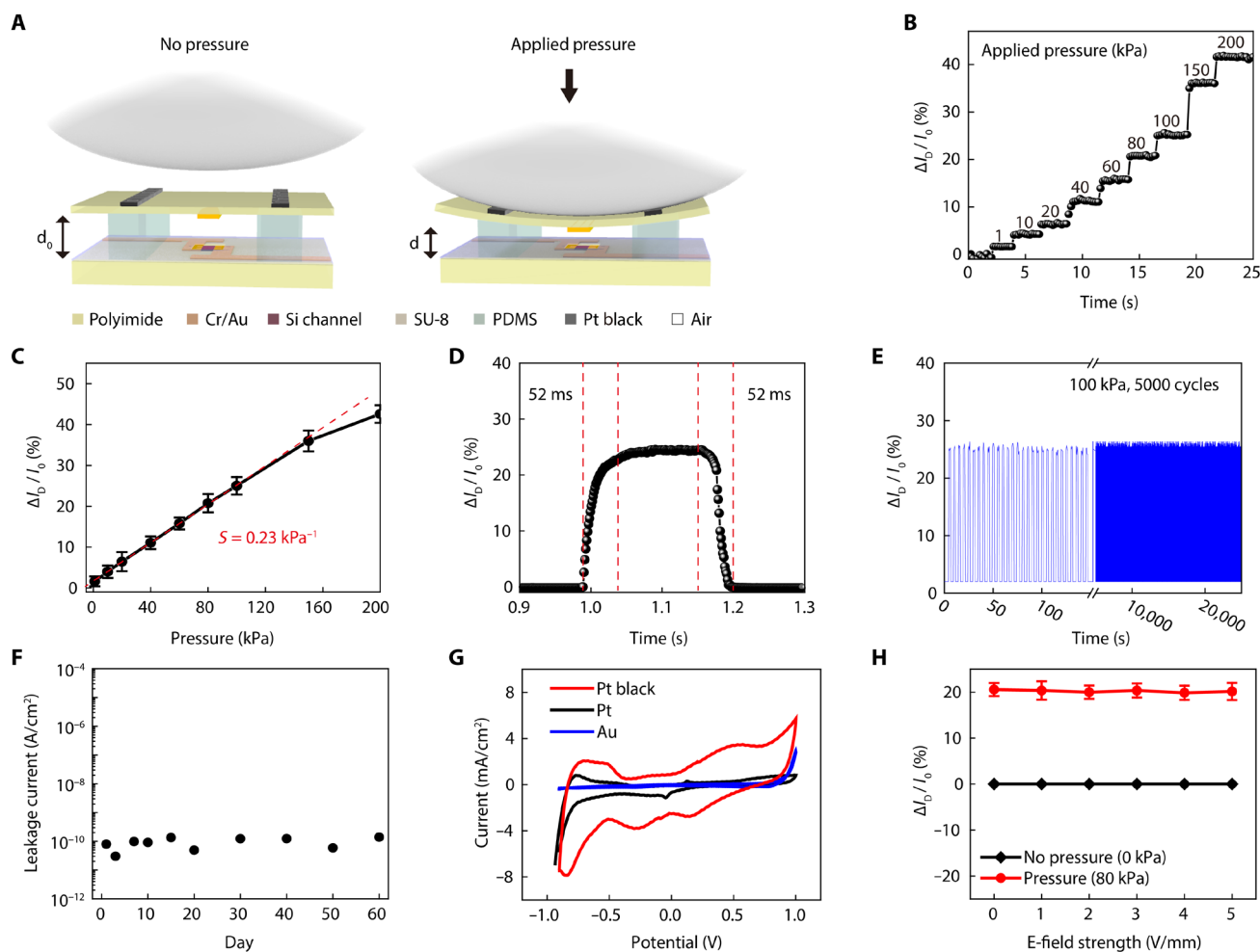
Fig. 2. Performances of the pressure-sensitive transistors and pacing electrodes. (**A**) Schematic layouts of an air-dielectric transistor and its operating mechanism as a compressive pressure sensor. (**B**) Real-time measurement of the relative change in I_D of the transistor when applying various pressures (at $V_G = 15$ V, $V_D = 1$ V). (**C**) Relative change in I_D by the applied compressive pressure. S denotes the pressure sensitivity. (**D**) Response and recovery time of the pressure-sensitive transistor during pressure loading (100 kPa) and unloading. (**E**) Relative change in I_D of the transistor with 5000 cyclic compressions to 100 kPa for testing its mechanical reliability. (**F**) Measurement of leakage currents of this device platform using an electrochemical impedance spectroscopy by its immersion in a PBS solution for 60 days. (**G**) Cyclic voltammetry plot of Au, Pt, and Pt black electrodes recorded at a sweep rate of 100 mV S^{-1}. (**H**) Dependence of the transistor signal ($\Delta I_D/I_0$) on the strength of the electric field generated at pacing electrodes.

force gauge (Mark-10 M7-20). Figure 2B shows the real-time detection of relative change in I_D [$\Delta I_D/I_0$ (%)], where I_0 is the current at zero Pascal and $\Delta I_D = I - I_0$, which denotes the variation of the I_D during stepwise pressure loading. This graph shows that the response to the applied pressure was distinguished clearly as a step-like response. The sensitivity (S) of this pressure-sensitive transistor was obtained by plotting the relative change in I_D concerning the applied pressure, and it was expressed as [I_D/I_0 (%)]/ΔP, where ΔP denotes the applied pressure. $\Delta I_D/I_0$ increased linearly within the pressure range from 1 to 150 kPa, where the sensitivity was calculated as 0.23 kPa^{-1} (Fig. 2C). The signal-to-noise (SNR) can be defined as SNR = μ/σ, where μ is the averaged value of relative I_D when the pressure (1 kPa) is loaded, and σ is the SD of the noise levels when the pressure is unloaded. In our sensor, SNR was measured to be ~13 when the 1 kPa of the pressure was loaded to the pressure-sensitive transistor. The minimum pressure sensing level can be calculated to be ~77 Pa, according to the measured SNR. A table of comparison with the characteristics and performances of pressure sensors in biomedical applications is shown to differentiate this device (table S2).

In addition, this pressure-sensitive transistor exhibited fast response and recovery time (~52 ms) with negligible hysteresis (Fig. 2D). To monitor heartbeats with dynamic cardiac motions, we need to secure reliable operation of this transistor during the repetitive application of pressure. Figure 2E shows that this transistor operated stably; it had negligible change in signals ($\Delta I_D/I_0$) after 5000 cycles of repetitive pressure loading at 100 kPa. In addition, this flexible, patch-like platform was attached to the outer surfaces of cylinders with various radii to test the flexibility and bending endurance of this epicardial patch. Figure S2A shows the negligible change in I_D during its mechanical bending with various curvatures from 5 to 30 mm, where these curvatures are sufficiently small compared to the case of the cardiac short-axis range of an adult rabbit (~30 mm) (35). In addition, there was no notable change in the signal ($\Delta I_D/I_0$) after 5000 cycles of repeated bending to 10 mm of radius (fig. S2B) due to thin thickness, reducing its bending stiffness (36).

For implantable electronic biomedical devices, the electrical leakage (that can be caused by environmental factors or insufficient insulations) is one of the biggest challenges (37). In particular, in the case of a heart, the leakage current generated by implantable devices can induce complications, such as ventricular fibrillation and heart failure, which can be fatal. For this reason, the leakage current of an implantable electronic device should be less than 10 μA (38–40). To measure the leakage current of our device platform, we performed a 60-day shock test (15) by submerging it in phosphate-buffered saline (PBS) solution and then measuring its leakage current using electrochemical impedance spectroscopy (EIS) with a Pt reference electrode. As shown in Fig. 2F, the leakage current was measured to be less than 1 nA, which was small enough for the leakage current of an epicardial bioelectronic patch, and the operation of the device (with applying 3-V DC bias) at ambient condition for 60 days did not increase this leakage current. In addition, long-term stability in biofluids was tested to ensure the reliable operation of the air-dielectric transistor in wet condition. For this test, the patch device was immersed inside a water and PBS solution (pH 7.4) and then maintained at the temperature of ~37°C, which corresponded to the body temperature, for up to 30 days. Then, the performance of the air-dielectric transistor was checked. As shown in fig. S3, our patch device continuously operated with negligible degradations in both

water and PBS solution for up to 30 days. The complete encapsulation of the patch-like platform using biocompatible passivation materials (silicone and parylene) was effective in achieving this negligible leakage current, and, in contrast to conventional electrophysiological devices, no electrodes of the active-matrix transistor array had to be exposed to the surrounding tissues for monitoring cardiac pressures.

As illustrated in Fig. 2A, the pacing electrodes for cardiac electrical stimulation were located above the top layer of pressure-sensitive transistors. These pacing electrodes were coated selectively by Pt black as a biocompatible metal with nanometer-scale rough surfaces. Because of the increase of its surface area, the low impedance and high CSC of this Pt black coating enabled excellent charge injection characteristics, thereby enhancing the pacing efficiency while minimizing the damage to the biological tissue (41). For example, EIS and cyclic voltammetry were used to compare the impedance and CSC characteristics of three different metallic electrodes using Au (evaporated), Pt (evaporated), and Pt black (electroplated) by their immersion in 0.1 M PBS (pH 7.4) at 25°C. During these tests, the dimensions of the electrodes of these three metals, i.e., Au, Pt, and Pt black, were identical, i.e., 0.6 mm^2. This test was performed using the standard three-electrode configuration (reference, Ag/AgCl; counter, Pt wire; and the working electrode, the tested metal). As plotted in fig. S4A, these electrodes of Pt black, Pt, and Au exhibited impedance values (at 10^3 Hz) of 81.3, 156.9, and 383.6 Ω, respectively. As shown in the scanning electron microscopy image of fig. S4B, this Pt black sample showed the formation of Pt nanoclusters with rough surfaces, which was in clear contrast to the smooth surfaces of the other Pt or Au films deposited by thermal evaporation. The Pt black electrode had the lowest impedance among these three samples because of its high surface area. In addition, this Pt black showed an outstanding charge storage characteristic, which was about 6.4 times higher than that of the Au electrode (Fig. 2G). This low impedance and high CSC of pacing electrodes using Pt black can enhance the electrode-to-cell signal transfer, which can be advantageous for cardiac stimulation. The mechanical and electrochemical stability tests of the electroplated Pt black were conducted. In this mechanical stability test, the cyclic voltammograms of Pt black were insignificantly changed by the scanning cycles, indicating that Pt black maintained its structure without noticeable exfoliation (fig. S5). For the electrochemical stability evaluation, we compared the impedance before and after by submerging Pt black in PBS in an incubator at 37°C for an hour. Figure S6 shows the negligible increase in impedance.

Furthermore, this patch-like platform can use these pacing electrodes to apply immediate electrical pulses when a disease-related abnormality is detected, while its continuous monitoring of cardiac motions continues using the pressure-sensitive transistors. Thus, the correlation between the distortion of the pressure signal (detected by the transistors) and the electrical pulses (generated by the pacing electrodes) should be validated. As shown in Fig. 2H, applying an electric field (from 0 to 5 V/mm) to the pacing electrodes of this patch-like platform for electrical stimulation did not change the signal ($\Delta I_D/I_0$) of the pressure-sensitive transistor when no pressure was applied. During the application of identical electric fields to the pacing electrodes, the transistor detected the application of compressive pressure (80 kPa) immediately without any interference with the signals.
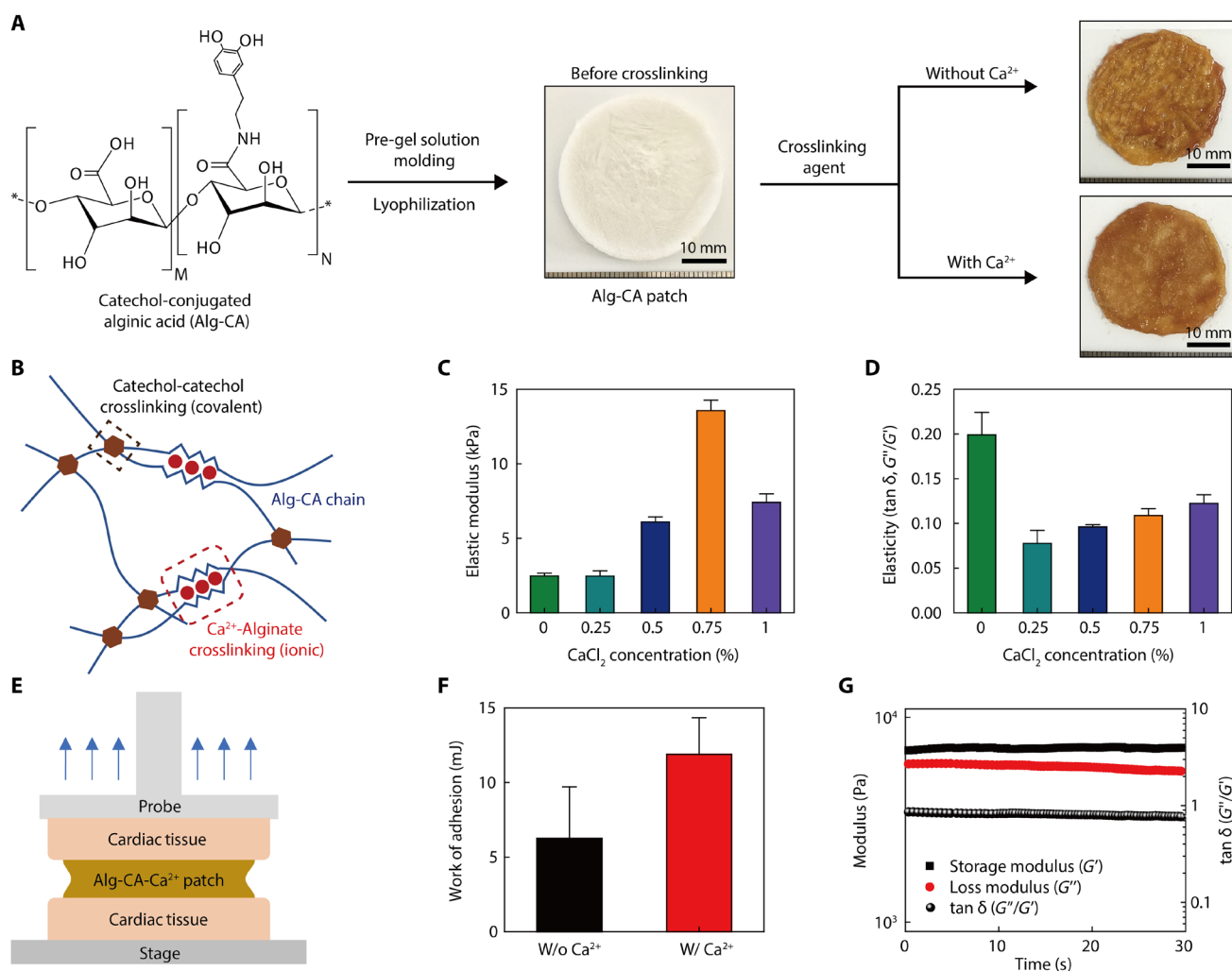
Characterizations of the Alg-CA-Ca^{2+} adhesive layer

A lyophilized, alginate-based adhesive was synthesized using a dual-crosslinking mechanism (covalent and ionic bonds) to strengthen

the conformable adhesion of this device platform onto the epicardium during beating heart motions without any separate surgical operation. In addition, this adhesive layer (as a patch form), which firmly covers the entire top surface of our device platform and the surrounding epicardium area, can act as its back-pressure support to amplify the recording signal of the pressure sensors. Following the strong adhesion of mussels in aqueous environments, a catechol-based hydrogel adhesive has been researched extensively (42–44). Its excellent adhesion to wet surfaces, including wet internal organs, has been an exciting topic (45). In addition, the outstanding biocompatibility of this alginate-based hydrogel and its nonresorbability in the body make it suitable for its use as a medical-grade adhesive (46) that can prevent the detachment of our device platform from a wet epicardium during cardiac beating motions. From these perspectives, a hydrogel adhesive was synthesized by introducing the catechol group to the alginate polymer chain, mimicking the mussels-like adhesive property, and was prepared in the form of a lyophilized

patch layer to improve the physical properties and facilitate its usage in clinical applications. Using this hydrogel adhesive patch, we can ensure secure and stable attachment of our device platform to the wet surface of a heart. In addition, Ca^{2+} was used as a crosslinking agent together with oxidant for this hydrogel because alginate naturally interacts with Ca^{2+} (47). Thus, the dual-crosslinking derived from the combination of covalent bonding (conjugated catechol group) and ionic bonding (Ca^{2+} ions) can synergistically increase the mechanical strength and adhesion of this alginate-based hydrogel adhesive.

Figure 3A shows the process of preparing this lyophilized hydrogel adhesive in the form of a patch. The synthesis steps of this alginate-catechol-calcium (Alg-CA-Ca^{2+}) adhesive patch are described in detail in the Supplementary Materials and in Materials and Methods. Since the fabrication process of the Alg-CA patch is quite straightforward and reproducible, uncontrollable influences on the device performance can be avoided when the Alg-CA patch is applied as the adhesive layer (fig. S7). As mentioned above, both

Fig. 3. Mechanical properties of the Alg-CA-Ca²⁺ adhesive patch. (**A**) Fabrication process of the alginate-based hydrogel adhesive patch. An adhesive patch, which is synthesized Alg-CA hydrogel, is prepared by lyophilization and then cross-linked by the spray of a crosslinking agent (oxidant, NaIO₄ solution containing Ca²⁺). (**B**) Schematic illustration of the dual-crosslinking mechanism (covalent and ionic) of the Alg-CA-Ca²⁺ adhesive. (**C** and **D**) Change in elastic modulus and elasticity of this adhesive by CaCl² concentration. (**E**) Schematic illustration of a probe tack test to measure the adhesion force of this Alg-CA-Ca²⁺ adhesive for porcine cardiac tissues. (**F**) Average work of adhesion of the Alg-CA-Ca²⁺ adhesive. (**G**) Viscoelastic properties of the adhesive and its endurance under the application of cyclic strains (oscillatory tensile strain, 30%; frequency, 2.5 Hz).

the alginate and catechol groups have a natural binding affinity with Ca^{2+}. When this adhesive patch was treated with Ca^{2+}, its mechanical strength was improved because of the dual-crosslinking reactions of the oxidative coupling between catechol groups and ionic bonding with Ca^{2+} (Fig. 3B). The elastic modulus that was analyzed using a rheometer of this adhesive exhibited a positive correlation with the Ca^{2+} concentration, and the highest modulus was observed at the concentration of 0.75% Ca^{2+} (Fig. 3C). This modulus was reduced as the Ca^{2+} concentration increased to 1% because the presence of excessive Ca^{2+} interfered with the binding of the catechol groups. Notably, as shown in fig. S8, the elastic modulus of this hydrogel patch (using the Alg-CA conjugate) prepared in a lyophilized form was higher than the cases of a bulk hydrogel formed using a solution form. This occurred because the internal structure was enhanced during the freezing step (48). The elasticity (tan δ) value of this adhesive was also improved when Ca^{2+} was present (Fig. 3D). Because of the enhancement of its storage modulus by Ca^{2+}, the adhesive can act as sturdy support that can increase the sensitivity of our pressure sensors during the relaxation of a heart. As shown in fig. S9, when this patch in a lyophilized state was treated with the crosslinking agent solution, this patch got soaked, allowing the stacked sheets to tightly interact with each other during interpolymeric crosslinking. Thus, the resultant cross-linked patch showed a much flatter shape and more compact structure than the lyophilized Alg-CA patch before crosslinking. The Alg-CA-Ca^{2+} patch cross-linked with both oxidizing agent and divalent cation has smoother surface morphology and more compact internal structure than the Alg-CA patch cross-linked with only oxidant agent solution without Ca^{2+} ion, which can be attributed to the dual-crosslinking reactions (covalent and ionic bonding) to make interpolymeric networks tighter and denser. As illustrated in Fig. 3E, we conducted a probe tack test using porcine cardiac tissue to evaluate the adhesion strength of this adhesive layer. After fixing the cardiac tissues on the surfaces of the stage and the probe, the tensile force was measured after bonding this adhesive layer between these two tissues through its crosslinking by oxidizing agents (with and without Ca^{2+}). Figure S10A shows this evaluation of the adhesion force between our adhesive patch and the porcine tissues. The interfacial force (yield point) was measured to be as high as ~7.5 N even in the presence of Ca^{2+} (fig. S10B). This interfacial force was induced mainly by its catechol group. In particular, as plotted in Fig. 3F, the work of adhesion was increased significantly after the Ca^{2+} treatment (~11.9 mJ), compared to the case without Ca^{2+} (~6.2 mJ). The noncovalent bonding (i.e., ionic bonding) of Ca^{2+} ions can contribute to the dissipation of energy inside the polymer, which improves the adhesion stability and mechanical strength of this adhesive (49, 50). This hydrogel adhesive patch provides sufficient tissue adhesiveness to mediate stable adhesion of the bioelectronic device on the epicardium, while it can be readily detached from this tissue without any lasting damage by simple actions such as peeling or rubbing. After detaching this adhesive patch from the heart tissue surface, histological analysis with hematoxylin and eosin (H&E) staining confirmed that there were no remnants of the adhesive patch and negligible damages on the tissue surface (fig. S11).

In addition, we also tested the mechanical durability of this adhesive patch to evaluate the impact of signal disruption during repetitive cardiac beating motions. Despite the repetitive application of 30% in the oscillatory tensile strain at a constant frequency of 2.5 Hz for 30 min using a rheometer, the mechanical properties of

this adhesive patch remained stable with negligible changes in the storage modulus, the loss modulus, and elasticity (Fig. 3G). Therefore, this Alg-CA-Ca^{2+} adhesive patch can offer reliable attachment of our single-device platform (with pressure sensors and pacing electrodes) to an epicardium that is undergoing repetitive and dynamic cardiac movements.

Motion detection using an artificial heart
We measured the beating motion of an artificial heart to evaluate the diagnostic capability of this device platform with the incorporation of an Alg-CA-Ca^{2+} adhesive patch. The half artificial heart was formed using a low-modulus silicone elastomer (Ecoflex 0030, Smooth-on Inc.) that has stiffness similar to that of a biological heart (51–53). The detailed experimental methods that were used to form this artificial heart are described in the Supplementary Materials. As illustrated in Fig. 4A, the device platform where the pressure-sensitive transistors and pacing electrodes were integrated was first placed near the central region of a pre-deflated artificial heart. Then, the entire top surface of this device platform and the surrounding epicardium area were covered by an Alg-CA-Ca^{2+} adhesive patch (thickness, 1 mm) that was cross-linked further by spraying an oxidizing agent (4.5 mg/ml $NaIO_4$ solution containing 0.75% $CaCl_2$). The cardiac beating characteristics such as local pressures and volume changes were evaluated by releasing the pigmented artificial blood in and out of this heart using a syringe pump. As shown in Fig. 4B, the internal pressure of this heart was measured using a digital manometer during the different pumping phases. While gradually increasing the volume of the artificial heart from 0 to 100%, the external pressure applied on the outer surface of the heart was also measured using a z-axis force gauge (Mark-10, M7-20) to set the reference. For comparison, the signal ($\Delta I_D/I_0$) of the pressure-sensitive transistor was monitored simultaneously. As plotted in fig. S12A, the expansion of this heart increased the external pressure up to ~80 kPa. In addition, the pressure-sensitive transistor that was attached to the heart using the Alg-CA-Ca^{2+} adhesive patch showed a larger increase in its signal ($\Delta I_D/I_0$) as the volume of the heart expanded, compared with the case without this adhesive (fig. S12B). Figure 4C shows the relationship between the value of the external pressure (measured using a gauge) and the $\Delta I_D/I_0$ of the transistor as the volume of the heart was increased. The transistor that was covered by the adhesive exhibited a 15-fold higher sensitivity of the signal ($\Delta I_D/I_0$) to the application of pressure, compared to the case without this adhesive (sensitivity: 0.2 kPa^{-1} with the adhesive, 0.013 kPa^{-1} without the adhesive). The sensitivity to the applied pressure (P), defined as ($\Delta I_D/I_0$)/ΔP, was calculated from the linear fit of the plot. Furthermore, to evaluate the sensing reliability of the pressure-sensitive transistor, this device that was attached to the artificial heart by the adhesive was subjected to a test that involved cycles of contraction and relaxation by repeatedly injecting and discharging artificial blood 1000 times using an automated syringe pump. Even after repeating 1000 cycles to 50 kPa, the change in its signal ($\Delta I_D/I_0$) was negligible, as shown in Fig. 4D.

Figure 4E shows a schematic illustration of a normal heart and LV hypertrophy (LVH) case. LVH, a condition in which the LV wall becomes enlarged and thickened, is caused by various cardiac conditions, such as hypertension, stenosis of the aortic valve, and insufficiency of the mitral valve (54–57). Although LVH has been diagnosed using electrocardiography and echocardiography, conventional electrocardiography is not suitable for diagnosing anatomic LVH of
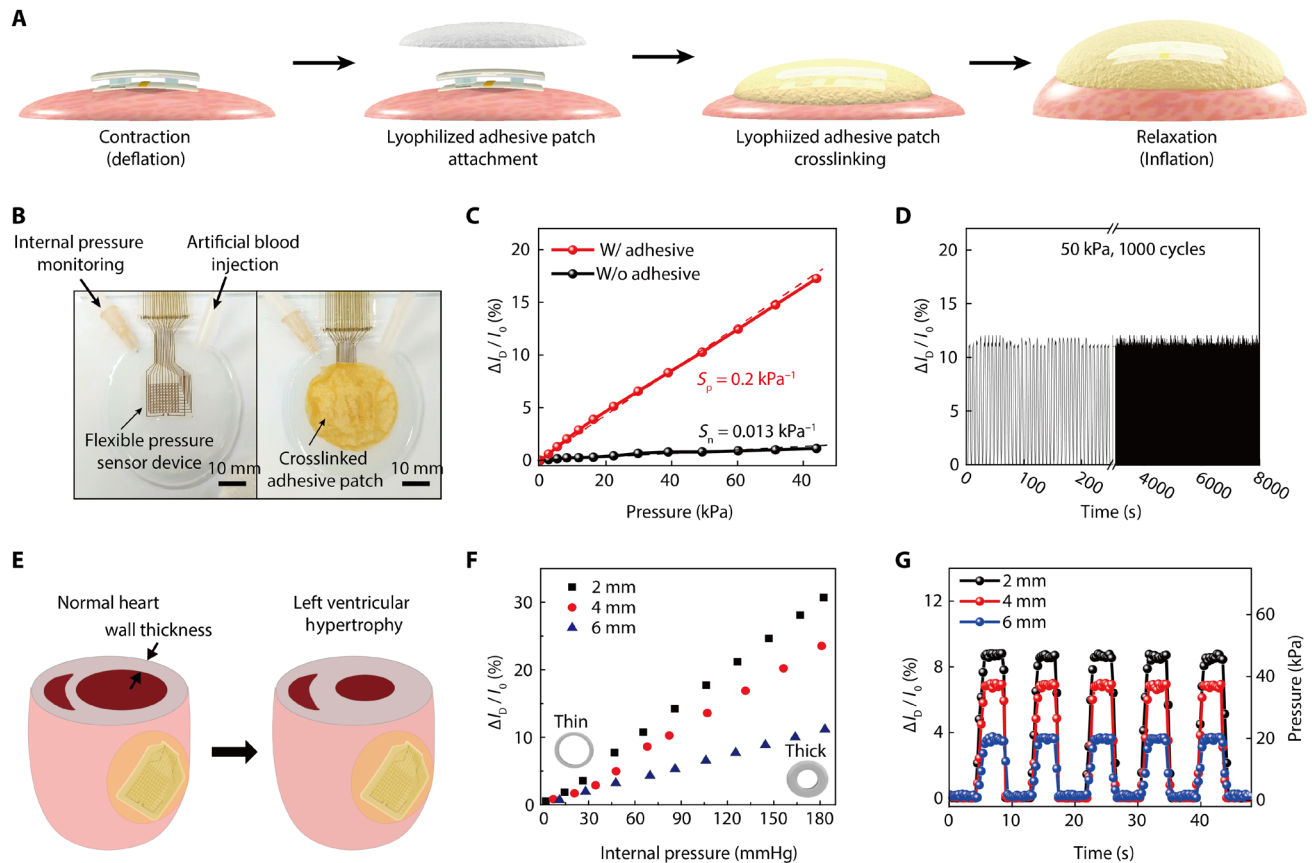
Fig. 4. Detection of beating motions using an artificial heart. (**A**) Schematic illustrations of cardiac contraction (deflation) and relaxation (inflation) with the attachment of our device platform (with the Ag-CA-Ca^{2+} hydrogel adhesive). (**B**) Photographs of this experimental setup to evaluate motion detections using the artificial heart. The black arrows indicate an injection tube of artificial blood and a needle tube for monitoring the internal pressure using a digital manometer. (**C**) Linear change in the transistor signal ($\Delta I_D/I_0$) by the pressure applied to the heart. Here, the pressure of this artificial heart was measured by a z-axis force gauge according to the volume incrementation of this heart. (**D**) Change in the transistor signal ($\Delta I_D/I_0$) under repetitive cycles of contraction and relaxation at 50 kPa (volume expansion of 80%) for 1000 cycles. (**E**) Schematic illustrations on a normal heart (left inset) and LV hypertrophy heart (right inset). (**F**) Dependence of the transistor signal ($\Delta I_D/I_0$) on the thickness of artificial heart wall with varying internal pressures. (**G**) Real-time measurement of the transistor signal ($\Delta I_D/I_0$) with three different thicknesses of artificial heart walls under repetitive cycles of their contraction and relaxation (from 0 to 50 kPa).

a heart (*58*–*60*). In addition, echocardiography is an expensive technique and is only available in hospitals, which is not suitable for real-time diagnosis in the patient's daily life (*61*). In particular, it is important to provide real-time anatomical information of the heart for LVH diagnosis due to its seamless gradual development. Furthermore, it has been reported that the wall thickness directly influences the diastolic properties of the LV (*62*, *63*). The thickening of the LV increases its stiffness because it is unable to relax normally and fill with blood. In this respect, our mechanophysiological device platform inserted into the body can intuitively provide real-time information regarding any anatomical progression related to the thickness of the LV wall by recording the change in epicardial pressures. The modeling of LVH disease can be simulated using artificial hearts with various wall thicknesses. To estimate LVH, half artificial hearts with three different wall thicknesses (2, 4, and 6 mm) were formed with identical outer diameters (70 mm). Then, our device platform with the pressure-sensitive transistor was attached to the surface of artificial hearts using the Alg-CA-Ca^{2+} adhesive patch to monitor $\Delta I_D/I_0$ when the blood flow pressure (BFP) of the internal artificial heart was applied by injecting artificial blood. This injection

of artificial blood increased the internal BFP value with a volumetric expansion of the heart, and this also led to the increase in $\Delta I_D/I_0$ of the pressure-sensitive transistor, as shown in Fig. 4F. Furthermore, the heart sample with the thinner wall thickness exhibited higher sensitivity of $\Delta I_D/I_0$ to the applied internal BFP (fig. S13). In addition, we measured the time-dependent change in signals ($\Delta I_D/I_0$) from these three different heart samples by repeating their contraction-relaxation cycles for respective systole and diastole conditions (Fig. 4G). When the BFP was increased repeatedly to 50 mmHg, the data were used to plot a real-time $\Delta I_D/I_0$ detection curve, i.e., Fig. 4G, and it represented a step-like feature. The recovering behavior in pressure sensing with negligible hysteresis was exhibited during the repeated contraction-relaxation cycle. Among these three heart samples, the increase in $\Delta I_D/I_0$ became larger with thinner wall thickness. Thus, the external pressure change recorded by our transistor can be associated to the ventricular thickness in the state of LVH. With respect to the clinical importance, this measurement of epicardial pressures can offer a promising potential for monitoring ventricular conditions associated with LVH while the heart is beating.

In vivo monitoring of cardiac motions in a live rabbit model

To examine the potential of this device platform (with pressure-sensitive transistors and pacing electrodes) for monitoring cardiac beating motions, we conducted in vivo tests using a live rabbit model (New Zealand white rabbit, male, 3.0 kg). To stably attach this patch device to the rapidly beating heart [~180 beats per minute (bpm)], the heart rate of anesthetized rabbit was temporarily slowed by esmolol (Jeilpharm Inc.) injection via the marginal vein of the ear at a rate of 0.5 mg kg^{-1} min^{-1}, which is a short-acting intravenous

cardioselective β-adrenergic blocker used for the short-term control of ventricular rate (64). This flexible patch device was attached to the epicardial surface of the anterior LV of rabbit in time for the systole phase when the heart rate dropped below ~60 bpm. Then, this patch device was covered completely by the Alg-CA-Ca^{2+} adhesive patch and rapidly cured using crosslinking agent with oxidant (Fig. 5, A and B). After fixing this patch device to the LV surface, the normal heart rate was successfully restored. Through this esmolol treatment, it was possible to minimize the difference in the recording
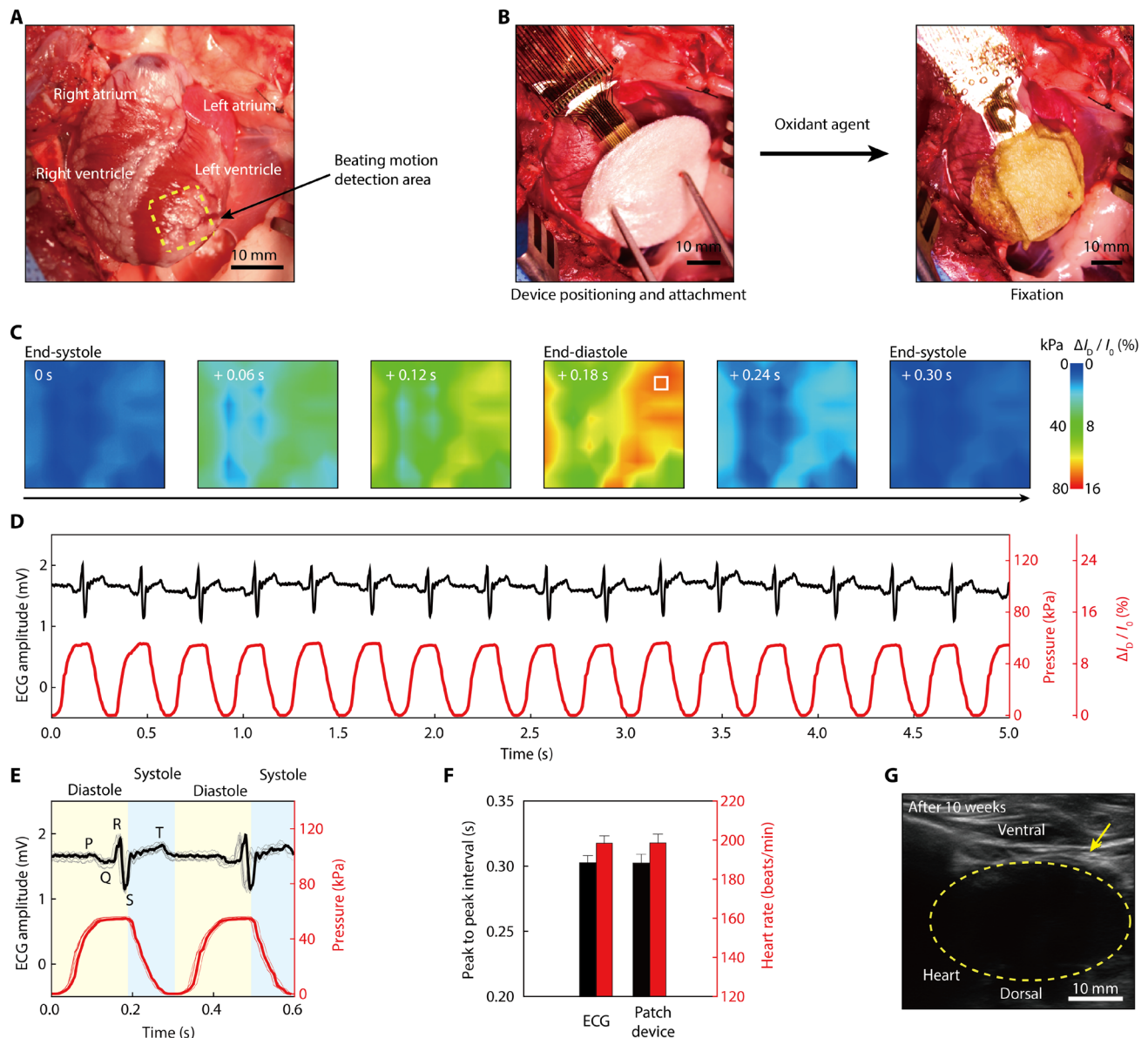
Fig. 5. Real-time monitoring of cardiac beating motion in a live rabbit model. (**A**) Photograph of a live rabbit heart before the attachment of the device platform. Four chambers of this heart are shown in the photograph. The yellow dashed box indicates the site for the motion detection area using this patch-type device. (**B**) Photographs of the attachment process. The device patch was attached to the LV epicardium by covering an Ag-CA-Ca^{2+} adhesive. (**C**) Spatiotemporal color maps of epicardial pressure distribution measured using this device platform during a single cardiac cycle of a normal anesthetized rabbit. (**D**) Real-time detection trace of epicardial pressures (red line) using a pressure-sensitive transistor in the device platform [indicated by the white box at the end-diastole 2D map of (C)], in comparison to the surface ECG trace (black line). (**E**) Overlapped traces of epicardial pressures and the surface ECG, distinguishing the diastole and systole phases of a rabbit's heart. (**F**) Comparison of heart rates and the peak-to-peak interval derived from the pressure sensing and the surface ECG. (**G**) Ultrasound image of the patch-type device platform attached to the epicardium of a rabbit's heart for 10 weeks.

value that is based on the irregularity of the cardiac phases when attaching the patch device. For example, as shown in fig. S14, stable cardiac surface pressure values were obtained even in repeated experiments (five times) through the treatment with esmolol. Then, the spatiotemporal distribution of epicardial pressures was mapped directly by monitoring the resultant signal ($\Delta I_D/I_0$) of each transistor during cardiac beating motions. Simultaneously, this measured pressure change was compared with the surface ECG trace obtained using a three-lead ECG module (PhysioLab Co., Korea). The experimental method for this ECG recording is detailed in Materials and Methods. Figure S15 shows photographs of the surgical preparation. In addition, the data acquisition (DAQ) setup and circuit diagram of 100 active-matrix array for the in vivo animal experiment are shown in fig. S16.

Similar to Fig. 4C, each transistor's signal magnitude ($\Delta I_D/I_0$) was converted to the relative pressure change with the sensitivity of 0.2 kPa^{-1}. Figure 5C presents spatiotemporal color contour plots of the pressure distribution of the normal, anesthetized rabbit during its cardiac beating motions. We have designed an array of pressure-sensitive transistors with its overall size of about 10 mm × 10 mm, a similar dimension to overlap the LV of a rabbit's heart. In this pressure mapping, the 10 × 10 active-matrix transistor array has a pixel resolution of 1 mm (that is, a total distance between adjacent transistors), which is based on the diameter of the left coronary arteries (rabbit, about 1 mm; human, 3 to 6 mm) and their branch vessels (65, 66). Movie S1 provides a video clip comparing this spatiotemporal plot of the pressure distribution (bottom right) with the corresponding surface ECG trace (top inset) over time during the rabbit's normal heartbeats. The conformal adhesion of this flexible device patch on the epicardium ensured its reliable monitoring of pressures during continuous systole and diastole cycles without its delamination. For example, Fig. 5D plots a real-time trace of the relative pressure change detected from a single pixel of pressure-sensitive transistor (indicated by the white box at the end-diastole 2D map in Fig. 5C) of this device platform in cardiac cycles. This pressure trace was consistent with the ECG trace to indicate the identical heart rate. Figure 5E compares two representative traces of pressure and ECG on the same timeline in two cardiac beating cycles. The QRS complex peak of this ECG trace clearly indicated the depolarization of the ventricular cardiomyocytes, signaling their contraction. Ventricular contraction pumped blood into the body, thereby subsequently reducing the volume of the chamber. Here, the corresponding pressure trace indicated the coincident reduction in the epicardial pressure at this end point of the QRS complex during the systole phase. In addition, the T wave of ECG revealed the ventricle's repolarization during ventricular relaxation. The pressure trace plotted the gradual increase in the epicardial pressure after this T wave. In addition, the heart rate obtained using the pressure-sensitive transistor was calculated on the basis of the time interval between consecutive systole peaks by differentiating this pressure plot, as shown in fig. S17. Then, it was compared with the heart rate detected by the surface ECG by calculating the time interval between the R peaks. Both sets of data (i.e., the pressure sensing and ECG sets) indicated identical values of the heart rate and peak-to-peak interval, as shown in Fig. 5F. Heart rate calculations were based on the previously reported assessment on heart rate variability (67). The duration of the diastole and systole were 0.19 and 0.11 s, respectively.

When an electronic cardiac patch is attached to the epicardium, the body can react to the device, so it is essential to assess the biocompatibility of an implantable electronic device. The biocompatibility of our device platform was tested by attaching it to the epicardium of a live rabbit using the hydrogel adhesive, and we routinely checked the abnormal cardiac functions and general health status of this rabbit for 10 weeks (fig. S18A). As plotted in fig. S18B, this rabbit stably maintained the normal heart rates in the range between 145 and 180 bpm for 10 weeks after the insertion of the device. In addition, Fig. 5G shows an ultrasound image of the device platform that was attached reliably to the epicardium of this rabbit even after 10 weeks. Furthermore, the H&E staining and macrophage assay were tested to evaluate the subcutaneous tissue inflammation in this live rabbit at 10 weeks. Figure S19 (A and B) shows no notable indications of inflammatory infiltrate in the subcutaneous tissue surrounding the heart.

In situ sensing and simultaneous electrical pacing for arrhythmia treatment

Figure 6A shows a schematic illustration of the induction of cardiac diseases in a rabbit model by drug injection and electrical shock to simulate the expression of arrhythmias. For the treatment of arrhythmias, the pacing electrodes integrated in our device platform can generate electrical impulses to control a rabbit's heart rate. At the same time, the pressure-sensitive transistors continuously monitor its heart rhythm. In this experiment, the device platform was placed on the anterior of the LV to monitor the rabbit's heartbeat, and the pacing electrodes were positioned near the apex to transmit the electrical pulses directly to the Purkinje fibers (Fig. 6B). Then, the Alg-CA-Ca^{2+} adhesive patch covered the top surface of this device layer before its crosslinking using an oxidant agent. First, three different noble metals, i.e., Au, Pt, and Pt black, were tested as pacing electrodes (with the same shape) to compare their cardiac pacing performance. Electrical pacing with the pulse width of 1 ms was applied at 5 Hz while increasing the amplitude of the pacing pulses to the heart of the live rabbit, as plotted in Fig. 6C. The pacing threshold can be defined as the minimum pacing amplitude required to induce the contraction of the heart muscle, and the pacing thresholds of the Au, Pt, and Pt black electrodes were 2.0, 1.4, and 0.6 V/mm, respectively. Because of the increment of its surface area, the low impedance and high CSC of this Pt black enabled extraordinary pacing characteristics at the lowest pacing threshold among these three metals. The maximum pacing amplitudes of all the electrodes were capped at about 5 V/mm because applying the amplitude over 5 V/mm induced LV fibrillation (LVF), i.e., a rapid, irregular heart rhythm. While applying electrical pacing using the Pt black electrodes (pulse amplitude, 0.6 V/mm; frequency, 5 Hz; pulse width, 1 ms), the relative changes in the epicardial pressures and in the surface ECG traces were recorded simultaneously, as shown in Fig. 6D. Although the initial normal heartbeat was slower than 200 bpm before applying the electrical pacing pulse, the application of this electrical pacing synchronized both signals of pressure and ECG together by inducing a faster heart rate, i.e., 300 bpm (that corresponds to the 5-Hz frequency). Pacing spikes, which mean the vertical signals, represent the electrical stimulus of the pacing device during its electrical impulse condition. As shown in Fig. 6D, ventricular pacing spikes are visible before each QRS complex. However, the overlapping of pacing spikes with the QRS complex waveform on ECG can lead to the misinterpretation of cardiac activity, unnecessary medical treatment, and potentially fatal outcomes. In contrast to the ECG, the signal on epicardial pressures detected using
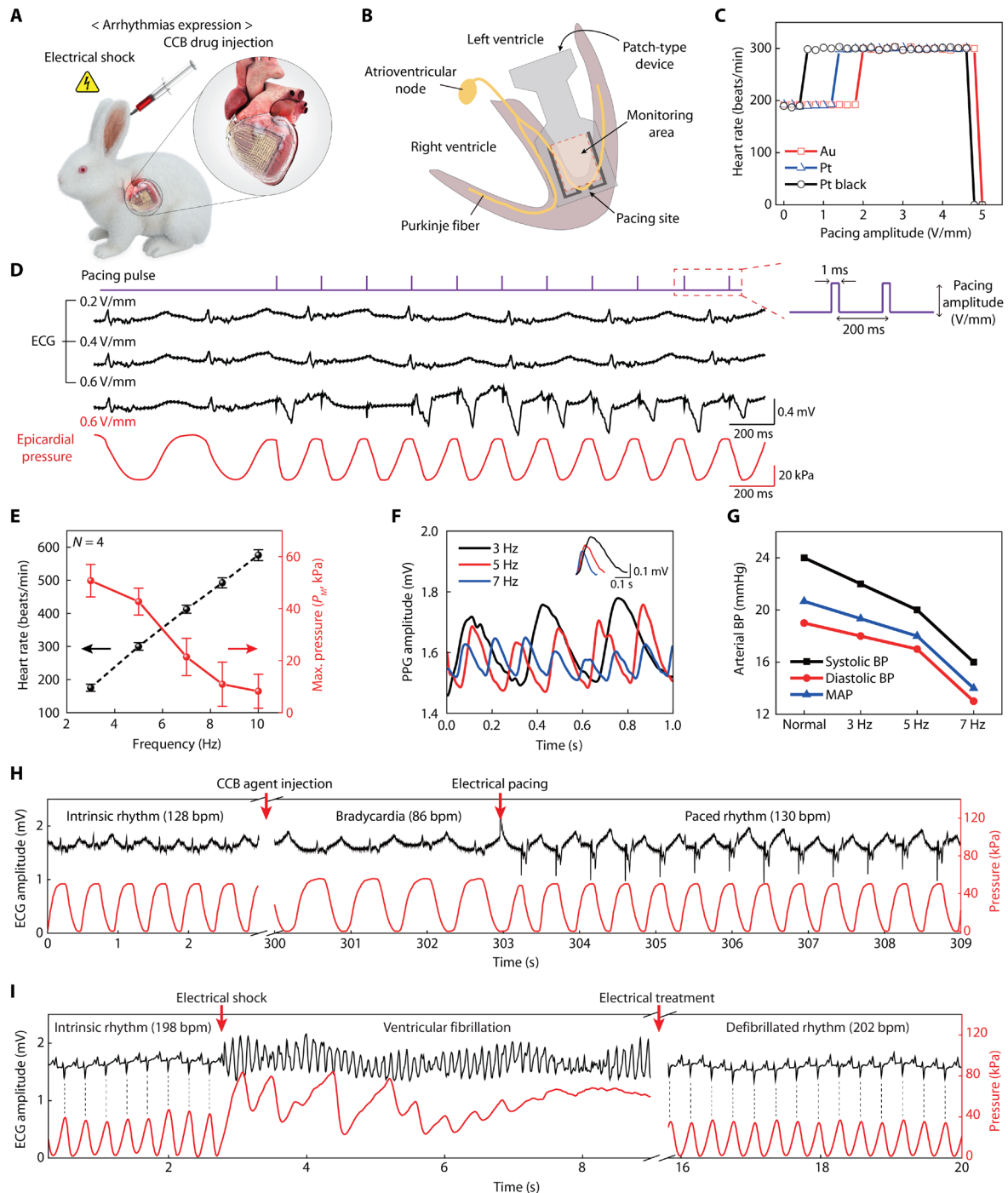
Fig. 6. In situ diagnosis and treatment of cardiac arrhythmia. (**A**) Schematic illustration on a live rabbit model for the arrhythmia expression by CCB drug injection and electrical shock. (**B**) Schematic illustration on the cross-section of a heart, indicating respective sites for the monitoring of cardiac beating motion and electrical pacing. (**C**) Electrical pacing characterization for successful heart rhythm modulation using three different pacing electrodes of Au, Pt, and Pt black (pacing condition: 5 Hz in frequency, 1 ms in pulse width). (**D**) Comparison between the surface ECG and epicardial pressure detection traces, according to pacing amplitude using the Pt black electrodes. (**E**) Synchronized heart rate and P_M measured by the device platform with respect to different pacing frequencies. (**F**) Real-time measurements of the photoplethysmogram at different pacing frequencies. The inset plots the magnified peaks of the photoplethysmogram, which compares the PPG amplitudes at different heart rates (3, 5, and 7 Hz). (**G**) Measurement of femoral arterial BP of the systole and diastole phases at different pacing frequencies. The mean arterial pressure values were calculated from the systole and diastole BP at respective pacing frequencies. (**H**) In situ diagnosis and simultaneous treatment of bradycardia using the device platform. Restoration to intrinsic heart rhythm after electric pacing (0.6 V/mm, 2.2 Hz, 1 ms) using the device platform was performed while continuously monitoring epicardial pressures (red line) and surface ECG (black line). (**I**) In situ diagnosis and simultaneous treatment of the expressed LV fibrillation using the device platform (red line), with comparison to the surface ECG trace (black line). For ventricular defibrillation, restoration to intrinsic heart rhythm by electrical treatment (7 V/mm, 1 s) was performed using this device platform. Dashed lines indicate the synchronized heartbeats between the ECG and pressure traces.

the pressure-sensitive transistor presented no pacing spike or any other interferences with the electrical stimulation pulses. Our device platform enabled mechanophysiological monitoring by detecting cardiac pressures instead of sensing electrical conduction (in the form of ECG), and this minimized the electromagnetic interferences between the sensing signals and the electrical pulses from the stimulators (i.e., pacing electrodes), as the form of a single-device system in which pressure sensors and pacing electrodes were integrated. Thus, this single platform can use its continuous recording of pressure to perform simultaneous, corrective treatment through immediate electrical impulses while monitoring the abnormal cardiac beating motions of arrhythmias.

As a control experiment to compare this signal interference effect, a flexible epicardial patch with arrays of Cr/Au electrodes (thickness, 5/60 nm) for epicardial ECG recording and Pt black electrodes for electrical pacing were fabricated separately, as illustrated in fig. S20. Then, these electrodes were encapsulated with a 500-nm-thick parylene layer with their opening (opening areas: 24 mm × 2 mm for ECG recording, 8 mm × 2 mm for pacing) for their direct contact with the surface of the epicardium. Subsequently, this epicardial patch was covered by the Alg-CA-Ca^{2+} adhesive for its strong adhesion to the rabbit's wet heart. Since this patch did not include any pressure sensors, it only enabled the electrophysiological test instead of mechanophysiological monitoring. Figure S21 shows the result of epicardial ECG recording with simultaneous electrical pacing using patch (pacing condition, 2 V/mm in pulse amplitude; 7 Hz in frequency; and 1 ms in pulse width). This patch regularly measured the bipolar epicardial electrogram amplitudes, which were dependent on the rabbit's heart rhythm, before initiating electrical pacing (time < 2.2 s on the x axis of fig. S21). However, as the electric pacing began, the electric pulses disrupted the ECG trace, rendering the interpretation of the ECG essentially impossible. In this electrophysiological patch, all electrodes for ECG recording and electrical stimulation were located on the wet surface of the epicardium, and this led to undesirable interference with the electric signals due to the leakage through the cardiac electrical conduction system and limited the simultaneous functions of ECG recording and cardiac pacing. In contrast, our mechanophysiological device system enabled the recording of cardiac beating motions by using pressure sensors with no signal disruption during the application of electrical impulses in electrical therapeutics.

During the operation of our mechanophysiological device system with pressure-sensitive transistors and pacing electrodes, the heart rate of this rabbit became synchronized according to the pacing frequency of the electrical stimulation (pulse amplitude, 0.6 V/mm; pulse width, 1 ms). As shown in Fig. 6E, the magnitude of the maximum pressure for each beat (P_M) decreased approximately five times as the paced heart rate increased from 175 bpm (corresponding to 3 Hz) to 576 bpm (10 Hz). The insufficient relaxation of the ventricle caused by the faster heart rate could result in this reduction in P_M due to the limitation in blood supply from the left atrium to the LV. Therefore, the shortened ventricular filling phase could lead to a decrease in the stoke volume. For example, the ventricular filling phase is shortened when the heart beats too fast (generally, a heart rate greater than 100 bpm in human adults) due to abnormal electrical pacing signals. These rapid heartbeats disrupt the filling of ventricles with blood, resulting in a lack of blood in the body, which is a condition known as ventricular tachycardia (68, 69). To compare this dependence of P_M on heartbeats, the relationship between the decrease in

blood flow and abnormally fast heart rates was tested further by the hemodynamic measurement of peripheral arteries using photoplethysmography (PPG). Here, a customized PPG sensor (PhysioLab Co., Korea) was attached to the sublingual artery of a rabbit's tongue to measure the change in the volume of blood (fig. S22A). To measure the arterial BP, we inserted a catheter integrated with the BP transducer into the femoral artery of the rabbit (fig. S22B). Insufficient blood flow from the ventricle to the rest of the body caused a reduction in arterial BP and a decrease of blood flow in the peripheral arteries. Figure 6F plots the resulting amplitude of PPG signal obtained from the sublingual artery during the electrical pacing of the rabbit's heart rate by varying frequency. Compared to its intrinsic heart rate (158 bpm on average) with no electrical stimulus, an application of electrical pacing frequency greater than 3 Hz induced faster heart rates to decrease further the amplitude of PPG and the relative flow rate of blood. Similarly, this increase in heart rates also reduced the BP of the femoral artery, i.e., the systolic, diastolic, and mean arterial pressure [diastolic BP + (systolic BP − diastolic BP)/3], due to insufficient blood flow from LV to the blood vessels (Fig. 6G). As a result, both measurements of epicardial pressure detection (using the pressure-sensitive transistor) and the hemodynamic analysis (using the PPG sensor) indicated the reduction in P_M and BP with increasing heart rates during electrical pacing.

Diltiazem (HERBEN, CJ Healthcare Inc.), a calcium channel blocker (CCB), inhibits the inflow of calcium ions into the cardiac muscle during depolarization, resulting in slowing of the SA node and a slowing conduction through the atrioventricular node. Thus, diltiazem causes sinus bradycardia (70). By injecting 4 ml of diluted CCB agent through the marginal ear vein of the rabbit at the rate of 1 ml/min, bradycardia became expressed in the rabbit with a reduction in its heart rate from 128 to 86 bpm. The electrophysiological and epicardial pressure traces were observed in the ECG and our device platform, respectively. To restore an intrinsic heart rate after this bradycardia expression, we paced this heart with the electrical pulse (amplitude, 0.6 V/mm; pulse width, 1 ms; frequency, 2.2 Hz) while monitoring its cardiac motions continuously. As shown in Fig. 6H and movie S2, this electrical pacing could recover the heart rate to an intrinsic condition of 130 bpm on average. To test further, we induced the LVF condition in the rabbit by using electrical shock. The subsequent variations in both surface ECG and epicardial pressure traces were compared during fibrillation (Fig. 6I). The ECG and pressure measurements verified the expression of LVF after applying excessive electrical pulses at a pulse amplitude of 5 V/mm, a frequency of 10 Hz, and a pulse width of 1 ms for 10 s. The surface ECG trace of the representative LVF wave, which was an irregular electrical activity with no discernible pattern, was plotted in Fig. 6I (black line; time range, 2.7 to 8.9 s). However, the consistent increase in epicardial pressure after the irregular pressure signal during LVF indicated that contraction of the LV did not occur, which were signs of asystole (red line in Fig. 6I; time range, 2.7 to 8.9 s). For defibrillation, we applied an electrical treatment for 1 s at a pulse amplitude of 7 V/mm using the pacing electrodes of this device platform while continuously monitoring the cardiac beating motions. The surface ECG and pressure traces after the defibrillation protocol, correcting the LVF, indicated that the intrinsic heart rhythm had been restored completely.

DISCUSSION
This study presents a heart-attachable single-device system that enables epicardial pressure detection and simultaneous electrical pacing

for in situ diagnosis and treatment of cardiac arrhythmias. This device platform consisted of an active-matrix pressure-sensitive transistor array with 10×10 sensing nodes, biocompatible pacing electrodes coated with Pt black nanoclusters, and an alginate-based hydrogel adhesive with negligible tissue inflammations. The pressure-sensitive transistors, as pressure sensors, enabled mechanophysiological analysis by continuously monitoring the spatiotemporal change in epicardial pressure distributions during heart beating motions. The Pt black–coated electrodes could control heart rates at a low pacing threshold (0.6 V/mm) due to their low impedance and high CSC characteristics. In addition, the biocompatible Alg-Ca-Ca^{2+} adhesive patch attached this device platform stably to the wet surface of a heart by improving the pressure sensitivity. In contrast to conventional electrophysiological methods such as ECG, this measurement of epicardial pressures enabled simultaneous treatment of electrical therapeutics using a single device without any interference between the sensing signals and electrical pulses from pacing electrodes, even in wet cardiac conditions. In vivo experiments using live rabbits have shown that this device platform can address arrhythmias, such as bradycardia and LVF, by monitoring abnormal heart rhythms and appropriately applying electrical treatment. Furthermore, the mechanophysiological detection of this device platform has offered a substantial potential for analyzing the physical properties of a heart related to the abnormalities of cardiac muscles and cardiovascular hemodynamics as well as providing deeper insights into the understanding of cardiac diseases and treatment. Thus, we envision that the results of this study can intuitively provide diverse and complex physiological information related to heart disease in complementary to the electrophysiological devices.

Although this epicardial device patch proposed in this work suggests a unconventional mechanophysiological analysis, only in vivo animal trials related to abnormal heart rhythms were studied. We expect that this mechanophysiological method using a similar device platform can expand the study of cardiac diseases to factors other than arrhythmias, such as myocardial infarction, hypertrophic cardiomyopathy, concentric hypertrophy, and dilated cardiomyopathy. To broaden the scope of its clinical applications, the permanent usability of this device platform with its completely wireless communications to external mobile systems and a self-sustainable, safe power source should be ensured further to adequately perform long-term assessments of organs and their functions. Together with the exploration of applications in various cardiac diseases and other areas, these and other functional improvements represent promising areas for future work.

MATERIALS AND METHODS
Experimental design
The purpose of this study was to develop a flexible, heart-attachable, device platform (as a patch shape) for monitoring cardiac beating motions and the simultaneous treatment of abnormal heart rhythms related to cardiac diseases. As a single-device system, this epicardial patch enabled the detection of epicardial pressures during cardiac beating cycles as well as the appropriate electrical pacing with no signal interference to each functional operation. This device platform comprises three components, i.e., (i) pressure-sensitive transistors (as pressure sensors), (ii) pacing electrodes, and (iii) an alginate-based hydrogel adhesive patch. The active-matrix array of pressure-sensitive air-dielectric transistors was used to record cardiac beating motions while visualizing the spatiotemporal distributions of the

epicardial pressures in real time. In addition, Pt black electrodes were integrated into this device system to transmit the electrical impulses needed for cardiac pacing. Moreover, a biocompatible hydrogel adhesive was developed to attach this device patch conformally to the epicardium for its reliable operation. To verify the capability of using this device platform to sense epicardial pressures, first, we formed and tested the artificial hearts before the in vivo trials using live rabbits. To further test the device's applicability, we conducted in vivo animal experiments using specific pathogen–free New Zealand white rabbits (total, $n = 6$). All of the animal experiments were conducted under the guidance of a cardiologist (S.L.). To detect the cardiac beating motions of live rabbits, we attached this flexible device patch to the epicardium of the LV of the anesthetized rabbits. To compare the characteristics of pacing electrode materials, three different metals, i.e., Pt, Au, and Pt black, were used as pacing electrodes for our device platform. Each of these was fabricated on an individual device. The pacing conditions (amplitude, frequency, and pulse width) and mechanophysiological test results using our device were compared by randomly selecting four rabbits and subjecting them to the experiments for surface ECG recording and pressure recording for 10 s. To evaluate the biocompatibility further, we attached this patch device to the epicardium of two anesthetized rabbits and left it there for 10 weeks. After 10 weeks, the two rabbits were subjected to a series of medical examinations. They were tested for inflammatory responses to the subcutaneous tissues surrounding their hearts, where the patch devices were attached for 10 weeks. Last, a CCB drug was injected, and an excessive electrical impulse was delivered into an anesthetized rabbit for bradycardia and LV fibrillation expression. To normalize the heart rate, we transmitted systematic pacing, and the pacing electrodes in our device platform transmitted defibrillating shock.

Fabrication of the patch device platform
For the fabrication of this bottom panel, a single-crystalline Si layer (thickness, 160 nm), which serves as the channel of the transistor, is transferred to a flexible polyimide (PI) film (thickness, 8 μm) from a silicon-on-insulator wafer (buried oxide, 400 nm) using a PDMS stamp. Source/drain/interconnect (5-nm Cr/100-nm Au) electrodes are deposited on the isolated Si channel using an e-beam evaporator (channel length, 40 μm; width, 150 μm). Then, this sample is covered by a 1-μm-thick photo-patternable epoxy layer (SU-8, MicroChem) with its opening above the channel region to form the locally vacant holes only inside this epoxy layer. This epoxy layer not only produces vacant regions on the Si channel at the designated positions but also passivates the source/drain/interconnect metallic electrodes. For the fabrication of this top panel, gate electrodes and interconnects (5-nm Cr/100-nm Au) are patterned photolithographically on a thin PI film (thickness, 3 μm) and then are covered by a PDMS elastomeric layer (thickness, 25 μm) in which vacant holes are pre-perforated locally using a laser ablation method (CO_2 laser, Epilog Laser Inc.). For the surface adhesive enhancement of the PDMS layer, this PDMS surface and the gate panel are exposed by O_2 plasma. The resulting bottom and top panels are laminated conformally with their precise alignment to combine the local holes in both layers of SU-8 and PDMS together, thereby completing the fabrication of a 10×10 active-matrix array of pressure-sensitive top-gate transistors with local air-dielectric layers. Here, the height of the air gaps can be determined by the total thickness of the two partition spacers (25-μm-thick PDMS and 1-μm-thick epoxy) between the channel

and the top-gate, and the thickness of this PDMS elastomeric layer can be decreased by applying compressive pressure with increasing capacitance of the gate-air-channel structure. This pressure-sensitive capacitance change enables the individual transistor to act solely as a single pressure sensor. Therefore, the simple integration of these transistors, with no additional component or layer, directly forms the active-matrix pressure sensor arrays, which can be advantageous because of the densification of these sensor arrays. To suppress the penetration of biofluids and to bind these two panels (top and bottom) in place, the entire sidewalls of this resulting sample are encapsulated completely by medical-grade silicone (Silastic MDX4-4210, Dow Inc.). After depositing a 100-nm-thick parylene encapsulation layer (as a biocompatible insulating layer) on the top surface of this sample, two pacing electrodes (ground and stimulation, respectively) are formed on this parylene surface using the evaporation of Cr/Au (thickness, 5 nm/60 nm) through a shadow mask. Sequentially, only these pacing electrodes are electroplated selectively by Pt nanoclusters (Pt thickness, 300 nm), which are referred to as Pt black. The advantage of this Pt black coating is that the addition of nanometer-scale roughness to these pacing electrodes can increase their surface area and lower their impedance greatly. The reduced impedance of pacing electrodes can enhance the electrode-to-cell signal transfer. Last, a 500-nm-thick parylene layer covers the entire surface of this sample again, leaving only the designated pacing site of Pt black electrodes uncovered locally (open area, 8 mm × 2 mm), which completes the fabrication of this thin and flexible patch-type platform where the active-matrix pressure sensor array and pacing electrodes are integrated (total thickness, 38 μm). Additional fabrication processes related to this flexible device patch are detailed in the Supplementary Materials.

Preparation and formation of the Alg-CA-Ca^{2+} adhesive patch

To prepare an Alg-CA patch, we dissolved the lyophilized Alg-CA conjugate in sterilized neutral PBS at a concentration of 1% (w/v) and then poured it onto a flat mold with the desired size and shape. This Alg-CA solution was completely lyophilized over 24 hours, producing an Alg-CA patch. To form an Alg-CA-Ca^{2+} patch, we placed it on the desired substrates or target tissue surfaces and we evenly sprayed it with a proper amount of crosslinking agents consisting of an oxidant (4.5 mg/ml of NaIO$_4$) and CaCl$_2$ (Sigma-Aldrich) at predetermined concentrations, i.e., 0, 0.25, 0.5, 0.75, and 1% (w/v).

Animal experiments

All of the animal experiments were approved by the Committee for Care and Use of Laboratory Animals at Yonsei University (College of Medicine), and the experiments were performed following the Guidelines for Institutional Animal Care and Use Committee (IACUC) of Yonsei University Severance Hospital (IACUC approval no. 2019-0275). The New Zealand white male rabbits (3.0 kg, Koatech, Korea) were injected intramuscularly with Rompun (5 mg/kg) and ketamine (20 to 30 mg/kg) to induce general anesthesia, and inhalation anesthetic (2% isoflurane) was administered to maintain the state of anesthesia. For the in vivo experiments, the sternum of a rabbit was incised vertically to expose the heart after disinfection. The pericardium was excised using an electrosurgical instrument. To consistently attach the device to the systole phase, heart rate was adjusted to beat slowly less than 60 bpm by administering esmolol (Jeilpharm Inc.) via the marginal vein of the ear at a rate of 0.5 mg kg^{-1} min^{-1}, while the heart rate was monitored using a separate medical ECG monitoring system. When the heart rate dropped below ~60 bpm, our device patch was positioned such that one side of this device was set to span the septum of the LV epicardium of the heart, while the stimulation electrode was placed on the Purkinje fiber of the LV near the apex. Then, this patch device was fixed by the Alg-CA-Ca^{2+} adhesive patch and rapidly cured by spray using crosslinking agent solution with oxidant. After about 20 min, the normal heart rate was successfully restored. During the in vivo recording of the surface ECG and pressure readouts, we have synchronized both datasets to a computer system time clock as they were simultaneously recorded. To verify the biocompatibility of this device platform, we inserted the epicardial bioelectronic patch into subcutaneous tissues. To confirm its stability, the position of this device was fixed on the epicardium using hydrogel adhesive, and subsequently, the incised chest was sutured shut. The rabbits used in the in vivo trials were euthanized humanely using KCl.

Measurement of surface ECG, PPG, and arterial BP

The electrical activity of live rabbits was recorded using a three-wire lead ECG system (PhysioLab Co., Korea). These three-lead wires were connected to commercial Ag/AgCl patches (3M Red Dot 2223) that were placed on the left and right chest (negative and ground) and femoral of the left leg (positive) on the exposed skin of a rabbit, respectively. The wires were connected to a separate ECG module with a signal filter. In addition, this ECG module was connected to a DAQ module to acquire real-time ECG traces, which were displayed through a LabVIEW-based customized software program. The sampling rate for recording the data was set at 1 kHz. For the hemodynamic measurement of peripheral arteries using PPG, a PPG sensor (PhysioLab Co., Korea) was connected to the DAQ module. Its sensing component was attached to the sublingual artery of the rabbit's tongue to record the real-time peripheral blood flow of the rabbit. Then, the arterial BP of the femoral of the rabbit was measured by the inserted catheter integrated with the pressure transducer.

Biocompatibility test

The biocompatibility of the patch device platform with the adhesive patch was histologically evaluated. The device platform and adhesive patch were inserted into the subcutaneous tissue surrounding the heart. After 10 weeks, subcutaneous tissue with the inserted device platform was cut for immunohistology analysis. The sliced sections of subcutaneous tissue were fixed in 10% formalin solution at 4°C for 24 hours. The paraffin blocks were made for H&E staining, and 4-μm-thick tissue sections were prepared for immunohistochemistry analysis with CD68 antibody (GTX34543, Gene Tex Co.) for macrophages.

Bradycardia induction

For bradycardia induction, 5 mg of diltiazem hydrochloride (HERBEN, CJ Healthcare Inc.) was diluted in 4 ml of saline (Sigma-Aldrich). The heart rhythm disturbances were evoked by the marginal ear vein administration of diltiazem solution to anesthetized rabbit. The ECG and epicardial pressure were recorded during intravenous injection of diltiazem solution, and the dosage was injected four times every minute. The ECG module and our device platform recorded real-time data that showed that the cardiovascular responses to diltiazem solution resulted in a heart rate of less than 90 bpm. After the bradycardia was stably induced for more than 30 s, application of electrical pacing started.

SUPPLEMENTARY MATERIALS

Supplementary material for this article is available at https://science.org/doi/10.1126/sciadv.abq0897

REFERENCES AND NOTES

1. S. S. Virani, A. Alonso, E. J. Benjamin, M. S. Bittencourt, C. W. Callaway, A. P. Carson, A. M. Chamberlain, A. R. Chang, S. Cheng, F. N. Delling, L. Djousse, M. S. V. Elkind, J. F. Ferguson, M. Fornage, S. S. Khan, B. M. Kissela, K. L. Knutson, T. W. Kwan, D. T. Lackland, T. T. Lewis, J. H. Lichtman, C. T. Longenecker, M. S. Loop, P. L. Lutsey, S. S. Martin, K. Matsushita, A. E. Moran, M. E. Mussolino, A. M. Perak, W. D. Rosamond, G. A. Roth, U. K. A. Sampson, G. M. Satou, E. B. Schroeder, S. H. Shah, C. M. Shay, N. L. Spartano, A. Stokes, D. L. Tirschwell, L. B. VanWagner, C. W. Tsao; American Heart Association Council on Epidemiology and Prevention Statistics Committee and Stroke Statistics Subcommittee, Heart disease and stroke statistics—2020 Update: A report from the American Heart Association. *Circulation* **141**, e139–e596 (2020).
2. A. S. Adabag, R. V. Luepker, V. L. Roger, B. J. Gersh, Sudden cardiac death: Epidemiology and risk factors. *Nat. Rev. Cardiol.* **7**, 216–225 (2010).
3. D. P. Zipes, H. J. J. Wellens, Sudden cardiac death. *Circulation* **98**, 2334–2351 (1998).
4. R. Mehra, Global public health problem of sudden cardiac death. *J. Electrocardiol.* **40**, S118–S122 (2007).
5. M. T. Keating, M. C. Sanguinetti, Molecular and cellular mechanisms of cardiac arrhythmias. *Cell* **104**, 569–580 (2001).
6. Task Force of the European Society of Cardiology the North American Society of Pacing Electrophysiology, Heart rate variability. *Circulation* **93**, 1043–1065 (1996).
7. A. J. Moss, W. J. Hall, D. S. Cannom, J. P. Daubert, S. L. Higgins, H. Klein, J. H. Levine, S. Saksena, A. L. Waldo, D. Wilber, M. W. Brown, M. Heo, Improved survival with an implanted defibrillator in patients with coronary disease at high risk for ventricular arrhythmia. *N. Engl. J. Med.* **335**, 1933–1940 (1996).
8. A. Mediratta, K. Addetia, M. Yamat, J. D. Moss, H. M. Nayak, M. C. Burke, L. Weinert, F. Maffessanti, V. Jeevanandam, V. Mor-Avi, R. M. Lang, 3D echocardiographic location of implantable device leads and mechanism of associated tricuspid regurgitation. *JACC Cardiovasc. Imaging* **7**, 337–347 (2014).
9. K. A. Polyzos, A. A. Konstantelias, M. E. Falagas, Risk factors for cardiac implantable electronic device infection: A systematic review and meta-analysis. *Europace* **17**, 767–777 (2015).
10. P. B. Nery, R. Fernandes, G. M. Nair, G. L. Sumner, C. S. Ribas, S. M. D. Menon, X. Wang, A. D. Krahn, C. A. Morillo, S. J. Connolly, J. S. Healey, Device-related infection among patients with pacemakers and implantable defibrillators: Incidence, risk factors, and consequences. *J. Cardiovasc. Electrophysiol.* **21**, 786–790 (2010).
11. X. Mei, K. Cheng, Recent development in therapeutic cardiac patches. *Front. Cardiovasc. Med.* **7**, 610364 (2020).
12. D.-H. Kim, R. Ghaffari, N. Lu, S. Wang, S. P. Lee, H. Keum, R. D'Angelo, L. Klinker, Y. Su, C. Lu, Y.-S. Kim, A. Ameen, Y. Li, Y. Zhang, B. de Graff, Y.-Y. Hsu, Z. Liu, J. Ruskin, L. Xu, C. Lu, F. G. Omenetto, Y. Huang, M. Mansour, M. J. Slepian, J. A. Rogers, Electronic sensor and actuator webs for large-area complex geometry cardiac mapping and therapy. *Proc. Natl. Acad. Sci. U.S.A.* **109**, 19910–19915 (2012).
13. L. Xu, S. R. Gutbrod, A. P. Bonifas, Y. Su, M. S. Sulkin, N. Lu, H.-J. Chung, K.-I. Jang, Z. Liu, M. Ying, C. Lu, R. C. Webb, J.-S. Kim, J. I. Laughner, H. Cheng, Y. Liu, A. Ameen, J.-W. Jeong, G.-T. Kim, Y. Huang, I. R. Efimov, J. A. Rogers, 3D multifunctional integumentary membranes for spatiotemporal cardiac measurements and stimulation across the entire epicardium. *Nat. Commun.* **5**, 3329 (2014).
14. J. Viventi, D.-H. Kim, J. D. Moss, Y.-S. Kim, J. A. Blanco, N. Annetta, A. Hicks, J. Xiao, Y. Huang, D. J. Callans, J. A. Rogers, B. Litt, A conformal, bio-Interfaced class of silicon electronics for mapping cardiac electrophysiology. *Sci. Transl. Med.* **2**, 24ra22 (2010).
15. H. Fang, K. J. Yu, C. Gloschat, Z. Yang, E. Song, C.-H. Chiang, J. Zhao, S. M. Won, S. Xu, M. Trumpis, Y. Zhong, S. W. Han, Y. Xue, D. Xu, S. W. Choi, G. Cauwenberghs, M. Kay, Y. Huang, J. Viventi, I. R. Efimov, J. A. Rogers, Capacitively coupled arrays of multiplexed flexible silicon transistors for long-term cardiac electrophysiology. *Nat. Biomed. Eng.* **1**, 0038 (2017).
16. J. Park, S. Choi, A. H. Janardhan, S.-Y. Lee, S. Raut, J. Soares, K. Shin, S. Yang, C. Lee, K.-W. Kang, H. R. Cho, S. J. Kim, P. Seo, W. Hyun, S. Jung, H.-J. Lee, N. Lee, S. H. Choi, M. Sacks, N. Lu, M. E. Josephson, T. Hyeon, D.-H. Kim, H. J. Hwang, Electromechanical cardioplasty using a wrapped elasto-conductive epicardial mesh. *Sci. Transl. Med.* **8**, 344ra86 (2016).
17. S.-H. Sunwoo, S. I. Han, H. Kang, Y. S. Cho, D. Jung, C. Lim, C. Lim, M. Cha, S.-P. Lee, T. Hyeon, D.-H. Kim, Stretchable low-impedance nanocomposite comprised of Ag–Au Core–shell nanowires and Pt black for epicardial recording and stimulation. *Adv. Mater. Technol.* **5**, 1900768 (2020).
18. J. Liu, X. Zhang, Y. Liu, M. Rodrigo, P. D. Loftus, J. Aparicio-Valenzuela, J. Zheng, T. Pong, K. J. Cyr, M. Babakhanian, J. Hasi, J. Li, Y. Jiang, C. J. Kenney, P. J. Wang, A. M. Lee, Z. Bao, Intrinsically stretchable electrode array enabled in vivo electrophysiological mapping of atrial fibrillation at cellular resolution. *Proc. Natl. Acad. Sci. U.S.A.* **117**, 14769–14778 (2020).
19. Y. S. Choi, R. T. Yin, A. Pfenniger, J. Koo, R. Avila, K. B. Lee, S. W. Chen, G. Lee, G. Li, Y. Qiao, A. Murillo-Berlioz, A. Kiss, S. Han, S. M. Lee, C. Li, Z. Xie, Y.-Y. Chen, A. Burrell, B. Geist, H. Jeong, J. Kim, H.-J. Yoon, A. Banks, S.-K. Kang, Z. J. Zhang, C. R. Haney, A. V. Sahakian, D. Johnson, T. Efimova, Y. Huang, G. D. Trachiotis, B. P. Knight, R. K. Arora, I. R. Efimov, J. A. Rogers, Fully implantable and bioresorbable cardiac pacemakers without leads or batteries. *Nat. Biotechnol.* **39**, 1228–1238 (2021).
20. P. Gutruf, R. T. Yin, K. B. Lee, J. Ausra, J. A. Brennan, Y. Qiao, Z. Xie, R. Peralta, O. Talarico, A. Murillo, S. W. Chen, J. P. Leshock, C. R. Haney, E. A. Waters, C. Zhang, H. Luan, Y. Huang, G. Trachiotis, I. R. Efimov, J. A. Rogers, Wireless, battery-free, fully implantable multimodal and multisite pacemakers for applications in small animal models. *Nat. Commun.* **10**, 5742 (2019).
21. A. Baranchuk, J. Kang, C. Shaw, D. Campbell, S. Ribas, W. M. Hopman, H. Alanazi, D. P. Redfearn, C. S. Simpson, Electromagnetic interference of communication devices on ECG machines. *Clin. Cardiol.* **32**, 588–592 (2009).
22. M. T. Liaquat, I. Ahmed, T. Alzahrani, *Pacemaker Malfunction* (StatPearls Publishing, 2022); https://ncbi.nlm.nih.gov/books/NBK553149/.
23. E. Cingolani, J. I. Goldhaber, E. Marbán, Next-generation pacemakers: From small devices to biological pacemakers. *Nat. Rev. Cardiol.* **15**, 139–150 (2018).
24. B. Nowak, Pacemaker stored electrograms: Teaching us what is really going on in our patients. *Pacing Clin. Electrophysiol.* **25**, 838–849 (2002).
25. C. Holmgren, T. Carlsson, C. Mannheimer, N. Edvardsson, Risk of interference from transcutaneous electrical nerve stimulation on the sensing function of implantable defibrillators. *Pacing Clin. Electrophysiol.* **31**, 151–158 (2008).
26. T. Shishido, M. Sugimachi, O. Kawaguchi, H. Miyano, T. Kawada, W. Matsuura, Y. Ikeda, T. Sato, J. Alexander, K. Sunagawa, A new method to measure regional myocardial time-varying elastance using minute vibration. *Am. J. Physiol.* **274**, H1404–H1415 (1998).
27. M. Han, L. Chen, K. Aras, C. Liang, X. Chen, H. Zhao, K. Li, N. R. Faye, B. Sun, J.-H. Kim, W. Bai, Q. Yang, Y. Ma, W. Lu, E. Song, J. M. Baek, Y. Lee, C. Liu, J. B. Model, G. Yang, R. Ghaffari, Y. Huang, I. R. Efimov, J. A. Rogers, Catheter-integrated soft multilayer electronic arrays for multiplexed sensing and actuation during cardiac surgery. *Nat. Biomed. Eng.* **4**, 997–1009 (2020).
28. E. T. Roche, M. A. Horvath, I. Wamala, A. Alazmani, S.-E. Song, W. Whyte, Z. Machaidze, C. J. Payne, J. C. Weaver, J. Fishbein, J. Kuebler, N. V. Vasilyev, D. J. Mooney, F. A. Pigula, C. J. Walsh, Soft robotic sleeve supports heart function. *Sci. Transl. Med.* **9**, eaaf3925 (2017).
29. M. Naveed, L. Han, G. J. Khan, S. Yasmeen, R. Mikrani, M. Abbas, L. Cunyu, Z. Xiaohui, Cardio-supportive devices (VRD & DCC device) and patches for advanced heart failure: A review, summary of state of the art and future directions. *Biomed. Pharmacother.* **102**, 41–54 (2018).
30. J. Jang, H. Kim, S. Ji, H. J. Kim, M. S. Kang, T. S. Kim, J. Won, J.-H. Lee, J. Cheon, K. Kang, W. B. Im, J.-U. Park, Mechanoluminescent, air-dielectric MoS$_2$ transistors as active-matrix pressure sensors for wide detection ranges from footsteps to cellular motions. *Nano Lett.* **20**, 66–74 (2020).
31. S. Ji, J. Jang, J. C. Hwang, Y. Lee, J.-H. Lee, J.-U. Park, Amorphous oxide semiconductor transistors with air dielectrics for transparent and wearable pressure sensor arrays. *Adv. Mater. Technol.* **5**, 1900928 (2020).
32. S.-H. Shin, S. Ji, S. Choi, K.-H. Pyo, B. Wan An, J. Park, J. Kim, J.-Y. Kim, K.-S. Lee, S.-Y. Kwon, J. Heo, B.-G. Park, J.-U. Park, Integrated arrays of air-dielectric graphene transistors as transparent active-matrix pressure sensors for wide pressure ranges. *Nat. Commun.* **8**, 14950 (2017).
33. J. Jang, B. Oh, S. Jo, S. Park, H. S. An, S. Lee, W. H. Cheong, S. Yoo, J.-U. Park, Human-interactive, active-matrix displays for visualization of tactile pressures. *Adv. Mater. Technol.* **4**, 1900082 (2019).
34. W. H. Cheong, B. Oh, S.-H. Kim, J. Jang, S. Ji, S. Lee, J. Cheon, S. Yoo, S.-Y. Lee, J.-U. Park, Platform for wireless pressure sensing with built-in battery and instant visualization. *Nano Energy* **62**, 230–238 (2019).
35. A. Moarabi, B. Mosallanejad, A. R. Ghadiri, R. Avizeh, Radiographic measurement of vertebral heart scale (VHS) in New Zealand white rabbits. *Iran. J. Vet. Surg.* **10**, 37–42 (2015).
36. L. Blanc, A. Delchambre, P. Lambert, Flexible medical devices: Review of controllable stiffness solutions. *Actuators* **6**, 23 (2017).
37. K. Bazaka, M. V. Jacob, Implantable devices: Issues and challenges. *Electronics* **2**, 1–34 (2013).
38. C. D. Swerdlow, W. H. Olson, M. E. O'Connor, D. M. Gallik, R. A. Malkin, M. Laks, Cardiovascular collapse caused by electrocardiographically silent 60-Hz intracardiac leakage current. *Circulation* **99**, 2559–2564 (1999).
39. M. M. Laks, R. Arzbaecher, J. J. Bailey, D. B. Geselowitz, A. S. Berson, Recommendations for safe current limits for electrocardiographs. *Circulation* **93**, 837–839 (1996).
40. Amendment of recommendations for standardization of specifications for instruments in electrocardiography and vectorcardiography concerning safety and electrical shock hazards. *IEEE Trans. Biomed. Eng.* **20**, 140–141 (1973).
41. Y. H. Kim, G. H. Kim, M. S. Kim, S.-D. Jung, Iridium oxide–electrodeposited nanoporous gold multielectrode array with enhanced stimulus efficacy. *Nano Lett.* **16**, 7163–7168 (2016).

42. J. Shin, J. S. Lee, C. Lee, H.-J. Park, K. Yang, Y. Jin, J. H. Ryu, K. S. Hong, S.-H. Moon, H.-M. Chung, H. S. Yang, S. H. Um, J.-W. Oh, D.-I. Kim, H. Lee, S.-W. Cho, Tissue adhesive catechol-modified hyaluronic acid hydrogel for effective, minimally invasive cell therapy. *Adv. Funct. Mater.* **25**, 3814–3824 (2015).

43. J. H. Ryu, J. S. Choi, E. Park, M. R. Eom, S. Jo, M. S. Lee, S. K. Kwon, H. Lee, Chitosan oral patches inspired by mussel adhesion. *J. Control. Release* **317**, 57–66 (2020).

44. R. Wang, J. Li, W. Chen, T. Xu, S. Yun, Z. Xu, Z. Xu, T. Sato, B. Chi, H. Xu, A biomimetic mussel-inspired ε-poly-l-lysine hydrogel with robust tissue-anchor and anti-infection capacity. *Adv. Funct. Mater.* **27**, 1604894 (2017).

45. W. Zhang, R. Wang, Z. Sun, X. Zhu, Q. Zhao, T. Zhang, A. Cholewinski, F. (K.) Yang, B. Zhao, R. Pinnaratip, P. K. Forooshani, B. P. Lee, Catechol-functionalized hydrogels: Biomimetic design, adhesion mechanism, and biomedical applications. *Chem. Soc. Rev.* **49**, 433–464 (2020).

46. K. Y. Lee, D. J. Mooney, Alginate: Properties and biomedical applications. *Prog. Polym. Sci.* **37**, 106–126 (2012).

47. A. Cholewinski, F. (K.) Yang, B. Zhao, Algae–mussel-inspired hydrogel composite glue for underwater bonding. *Mater. Horiz.* **6**, 285–293 (2019).

48. J. Shin, S. Choi, J. H. Kim, J. H. Cho, Y. Jin, S. Kim, S. Min, S. K. Kim, D. Choi, S.-W. Cho, Tissue tapes—Phenolic hyaluronic acid hydrogel patches for off-the-shelf therapy. *Adv. Funct. Mater.* **29**, 1903863 (2019).

49. C. H. Yang, M. X. Wang, H. Haider, J. H. Yang, J.-Y. Sun, Y. M. Chen, J. Zhou, Z. Suo, Strengthening alginate/polyacrylamide hydrogels using various multivalent cations. *ACS Appl. Mater. Interfaces* **5**, 10418–10422 (2013).

50. J.-Y. Sun, X. Zhao, W. R. K. Illeperuma, O. Chaudhuri, K. H. Oh, D. J. Mooney, J. J. Vlassak, Z. Suo, Highly stretchable and tough hydrogels. *Nature* **489**, 133–136 (2012).

51. W. Hiesinger, M. J. Brukman, R. C. McCormick, J. R. Fitzpatrick III, J. R. Frederick, E. C. Yang, J. R. Muenzer, N. A. Marotta, M. F. Berry, P. Atluri, Y. J. Woo, Myocardial tissue elastic properties determined by atomic force microscopy after stromal cell–derived factor 1α angiogenic therapy for acute myocardial infarction in a murine model. *J. Thorac. Cardiovasc. Surg.* **143**, 962–966 (2012).

52. C. Larson, B. Peele, S. Li, S. Robinson, M. Totaro, L. Beccai, B. Mazzolai, R. Shepherd, Highly stretchable electroluminescent skin for optical signaling and tactile sensing. *Science* **351**, 1071–1074 (2016).

53. J. G. Jacot, J. C. Martin, D. L. Hunt, Mechanobiology of cardiomyocyte development. *J. Biomech.* **43**, 93–98 (2010).

54. A. H. Gradman, F. Alfayoumi, From left ventricular hypertrophy to congestive heart failure: Management of hypertensive heart disease. *Prog. Cardiovasc. Dis.* **48**, 326–341 (2006).

55. M. Nakamura, J. Sadoshima, Mechanisms of physiological and pathological cardiac hypertrophy. *Nat. Rev. Cardiol.* **15**, 387–407 (2018).

56. S. Gunther, W. Grossman, Determinants of ventricular function in pressure-overload hypertrophy in man. *Circulation* **59**, 679–688 (1979).

57. B. A. Carabello, Concentric versus eccentric remodeling. *J. Card. Fail.* **8**, S258–S263 (2002).

58. W. B. Kannel, T. Gordon, W. P. Castelli, J. R. Margolis, Electrocardiographic left ventricular hypertrophy and risk of coronary heart disease. The Framingham study. *Ann. Intern. Med.* **72**, 813–822 (1970).

59. J. Siegrist, R. Peter, W. Motz, B. E. Strauer, The role of hypertension, left ventricular hypertrophy and psychosocial risks in cardiovascular disease: Prospective evidence from blue-collar men. *Eur. Heart J.* **13**, 89–95 (1992).

60. G. Schillaci, P. Verdecchia, C. Porcellati, O. Cuccurullo, C. Cosco, F. Perticone, Continuous relation between left ventricular mass and cardiovascular risk in essential hypertension. *Hypertension* **35**, 580–586 (2000).

61. J. Sundström, L. Lind, J. Ärnlöv, B. Zethelius, B. Andrén, H. O. Lithell, Echocardiographic and electrocardiographic diagnoses of left ventricular hypertrophy predict mortality independently of each other in a population of elderly men. *Circulation* **103**, 2346–2351 (2001).

62. W. Grossman, L. P. Mclaurin, S. P. Moos, M. Stefadouros, D. T. Young, Wall thickness and diastolic properties of the left ventricle. *Circulation* **49**, 129–135 (1974).

63. J. A. Wisneski, J. D. Bristow, Left ventricular stiffness. *Annu. Rev. Med.* **29**, 475–483 (1978).

64. D. Wiest, Esmolol. A review of its therapeutic efficacy and pharmacokinetic characteristics. *Clin. Pharmacokinet.* **28**, 190–202 (1995).

65. R. A. B. Burton, J. E. Schneider, M. J. Bishop, P. W. Hales, C. Bollensdorff, M. D. Robson, K. C. K. Wong, J. Morris, T. A. Quinn, P. Kohl, Microscopic magnetic resonance imaging reveals high prevalence of third coronary artery in human and rabbit heart. *Europace* **14**, v73–v81 (2012).

66. J. T. Dodge, B. G. Brown, E. L. Bolson, H. T. Dodge, Lumen diameter of normal human coronary arteries. Influence of age, sex, anatomic variation, and left ventricular hypertrophy or dilation. *Circulation* **86**, 232–246 (1992).

67. S. Sieciński, P. S. Kostka, E. J. Tkacz, Heart rate variability analysis on electrocardiograms, seismocardiograms and gyrocardiograms on healthy volunteers. *Sensors* **20**, 4522 (2020).

68. R. Wégria, C. W. Frank, H.-H. Wang, J. Lammerant, The effect of atrial and ventricular tachycardia on cardiac output, coronary blood flow and mean arterial blood pressure. *Circ. Res.* **6**, 624–632 (1958).

69. K. K. Steinbach, O. Merl, K. Frohner, C. Hief, M. Nürnberg, W. Kaltenbrunner, E. Wessely, Hemodynamics during ventricular tachyarrhythmias. *Am. Heart J.* **127**, 1102–1106 (1994).

70. J. Handler, Adverse effects using combined rate-slowing antihypertensive agents. *J. Clin. Hypertens.* **13**, 529–532 (2011).

71. S. E. Stanca, F. Hänschke, A. Ihring, G. Zieger, J. Dellith, E. Kessler, H.-G. Meyer, Chemical and electrochemical synthesis of platinum black. *Sci. Rep.* **7**, 1074 (2017).

72. C. Lee, J. Shin, J. S. Lee, E. Byun, J. H. Ryu, S. H. Um, D.-I. Kim, H. Lee, S.-W. Cho, Bioinspired, calcium-free alginate hydrogels with tunable physical and mechanical properties and improved biocompatibility. *Biomacromolecules* **14**, 2004–2013 (2013).

73. L. A. Kurup, C. M. Cole, J. N. Arthur, S. D. Yambem, Graphene porous foams for capacitive pressure sensing. *ACS Appl. Nano Mater.* **5**, 2973–2983 (2022).

74. C. M. Boutry, Y. Kaizawa, B. C. Schroeder, A. Chortos, A. Legrand, Z. Wang, J. Chang, P. Fox, Z. Bao, A stretchable and biodegradable strain and pressure sensor for orthopaedic application. *Nat. Electron.* **1**, 314–321 (2018).

75. C. M. Boutry, A. Nguyen, Q. O. Lawal, A. Chortos, S. Rondeau-Gagné, Z. Bao, A sensitive and biodegradable pressure sensor array for cardiovascular monitoring. *Adv. Mater.* **27**, 6954–6961 (2015).

76. X. He, Z. Liu, G. Shen, X. He, J. Liang, Y. Zhong, T. Liang, J. He, Y. Xin, C. Zhang, D. Ye, G. Cai, Microstructured capacitive sensor with broad detection range and long-term stability for human activity detection. *npj Flex. Electron.* **5**, 17 (2021).

77. S. Gong, W. Schwalb, Y. Wang, Y. Chen, Y. Tang, J. Si, B. Shirinzadeh, W. Cheng, A wearable and highly sensitive pressure sensor with ultrathin gold nanowires. *Nat. Commun.* **5**, 3132 (2014).

78. S. Kim, Y. Dong, M. M. Hossain, S. Gorman, I. Towfeeq, D. Gajula, A. Childress, A. M. Rao, G. Koley, Piezoresistive graphene/P(VDF-TrFE) heterostructure based highly sensitive and flexible pressure sensor. *ACS Appl. Mater. Interfaces* **11**, 16006–16017 (2019).

79. Y. Jeong, J. Park, J. Lee, K. Kim, I. Park, Ultrathin, biocompatible, and flexible pressure sensor with a wide pressure range and its biomedical application. *ACS Sens.* **5**, 481–489 (2020).

80. L.-W. Lo, H. Shi, H. Wan, Z. Xu, X. Tan, C. Wang, Inkjet-printed soft resistive pressure sensor patch for wearable electronics applications. *Adv. Mater. Technol.* **5**, 1900717 (2020).